Seismic attenuation tomography of the Mariana subduction system: Implications for thermal structure, volatile distribution, and slow spreading dynamics

Sara H. Pozgay

Department of Earth and Planetary Sciences, Washington University, 1 Brookings Drive, St. Louis, Missouri 63130, USA

Now at Research School of Earth Sciences, Australian National University, Building 61, Mills Road, Canberra, ACT 0200, Australia (sara.pozgay@anu.edu.au)

Douglas A. Wiens

Department of Earth and Planetary Sciences, Washington University, 1 Brookings Drive, St. Louis, Missouri 63130, USA

James A. Conder

Department of Earth and Planetary Sciences, Washington University, 1 Brookings Drive, St. Louis, Missouri 63130, USA

Now at Department of Geology, Southern Illinois University, Carbondale, Illinois 62901, USA

Hajime Shiobara

Earthquake Research Institute, University of Tokyo, 1-1-1 Yayoi, Bunkyo-ku, Tokyo, 113-0032 Japan

Hiroko Sugioka

IFREE, JAMSTEC, 2-15 Natsushima-Cho, Yokosuka, 237-0061 Japan

[1] The anelastic structure of a subduction zone can place first-order constraints on variations in temperature and volatile content. We investigate seismic attenuation across the western Pacific Mariana subduction system using data from the 2003–2004 Mariana Subduction Factory Imaging Experiment. This 11-month experiment consisted of 20 broadband stations deployed on the arc islands and 58 semibroadband ocean bottom seismographs deployed across the fore arc, island arc, and back-arc spreading center. We compute amplitude spectra for P and S arrivals from local earthquakes and invert for the path-averaged attenuation for each waveform along with the seismic moment and corner frequency for each earthquake. Additionally, we investigate earthquake source parameter assumptions and frequency-dependent exponents (α) ranging from 0 to 0.6. Tomographic inversion of nearly 3000 t^* estimates (at $\alpha = 0.27$) for 2-D Q_P^{-1} and Q_P/Q_S structure shows a $\sim$75 km wide columnar-shaped high-attenuation anomaly with $Q_P \sim 43$–60 beneath the spreading center that extends from the uppermost mantle to $\sim$100 km depth. A weaker high-attenuation region ($Q_P \sim 56$–70) occurs at depths of 50–100 km beneath the volcanic arc, and the high-attenuation regions are connected at depths of 75–125 km. The subducting Pacific plate is characterized by low attenuation at depths greater than 100 km, but high attenuation is found in the plate between 50 and 100 km depth. The fore arc shows high attenuation near the volcanic arc and beneath the serpentinite seamounts in the outer fore arc. Q_S structure is less well resolved than Q_P because of a smaller data set, but Q_P/Q_S ratios are significantly less than 2 throughout the study region. As temperatures

estimated from Q_S^{-1} are unusually high, we interpret the arc and wedge core anomalies as regions of high temperature with enhanced Q^{-1} due to hydration and/or melt, the slab and fore-arc anomalies as indicative of slab-derived fluids and/or large-scale serpentinization, and the columnar-shaped high Q_P^{-1} anomaly directly beneath the back-arc spreading center as indicative of a narrow region of dynamic upwelling and melt production beneath the slow spreading ridge axis.

1. Introduction

[2] The depth extent and distribution of temperature anomalies and fluids, including melt and slab-derived volatiles, within a subduction zone mantle wedge are of great importance for understanding subduction dynamics and back-arc spreading processes. Since geochemical studies find slab-derived volatiles and fluid-mobile elements at both the island arc and the back-arc spreading center [*Kelley et al.*, 2006; *Pearce et al.*, 2005; *Shaw et al.*, 2008], melt formation must be influenced by some volatile components that come from the slab. This first-order observation suggests a need to understand the spatial relationships of melt production and volatile transport regions between the slab and the volcanic front, the slab and the back-arc spreading center, and between the arc and the back-arc spreading center.

[3] There are also significant questions about spreading center dynamics that may be studied at back-arc spreading centers. Seismic imaging [*Forsyth et al.*, 1998; *Hammond and Toomey*, 2003; *Hung et al.*, 2000] shows that fast spreading centers are characterized by passive mantle upwelling, with melt produced over a broad region and transported to the mid-ocean ridge [e.g., *Sparks and Parmentier*, 1991; *Spiegelman and McKenzie*, 1987]. However, modeling studies suggest that melt formation at a mid-ocean ridge could also occur through a dynamic process in which low

viscosity and melt buoyancy would combine to produce a narrower focused upwelling beneath the ridge [e.g., *Su and Buck*, 1993]. Several studies suggest that upwelling dynamics at a spreading center might be dependent on the spreading rate, with slow spreading ridges exhibiting active dynamic upwelling and broad passive regimes for fast spreading ridges [*Madge and Sparks*, 1997; *Parmentier and Phipps Morgan*, 1990]. There is as yet no detailed mantle imaging beneath slow spreading centers to test this idea.

[4] An additional uncertainty at both the arc and back-arc mantle regions is the extent of in situ melt porosity. U-series disequilibria studies suggest the maximum melt content is very low (<0.1%), with melt presumably removed quickly and efficiently by porous flow [*Lundstrom et al.*, 1998; *Turner et al.*, 2001]. However, other studies suggest a much higher melt content within the melt producing regions of the upper mantle beneath arcs and spreading centers [*Faul*, 2001; *Hammond and Toomey*, 2003; *Nakajima et al.*, 2005].

[5] One subsurface imaging tool that can help to identify spatial variations in temperature, volatile content, and melt porosity is seismic attenuation. Experimental studies have shown that intrinsic seismic attenuation has an approximately exponential relationship with temperature [*Faul and Jackson*, 2005; *Jackson et al.*, 2002, 1992] and that volatiles dissolved in normally anhydrous mantle minerals can have a significant effect [*Aizawa et al.*, 2008;

Karato, 2003; *Shito et al.*, 2006]. In addition, recent laboratory experiments suggest that small amounts of melt porosity (<1%) have a significant effect on attenuation [*Faul et al.*, 2004]. As such, using seismic attenuation as an imaging tool in a subduction zone setting can provide constraints on thermal anomalies and variations in melt and volatile content.

[6] The Mariana subduction system shows both active island arc and back-arc volcanism and geochemical studies record slab-derived volatiles in the back-arc basin basalts [*Kelley et al.*, 2006; *Pearce et al.*, 2005]; as such, it presents an excellent location for mantle imaging studies. Here we exploit individual path-averaged *t** estimates recorded at seismographs from a well-distributed deployment of land and ocean bottom seismographs in 2003–2004 to determine seismic attenuation structure beneath the arc and back arc. We present the first seismic attenuation tomography images beneath a slow spreading ridge and discuss implications for thermal anomalies, volatile distribution, and the dynamics of the Mariana arc system.

2. Background

2.1. Regional Setting

[7] The northern Mariana subduction system encompasses a wide variety of tectonic settings with active serpentinite seamounts in the fore arc, an active island arc and back-arc spreading center, and an extinct arc on the overriding Philippine Sea Plate (Figure 1). The present study focuses on the region between 16 and 19.5°N, where the dip of the Jurassic-aged subducting Pacific Plate is nearly vertical at depths below 250 km and appears to penetrate the 660 km discontinuity [*van der Hilst et al.*, 1991]. A double seismic zone extends from ~60 to 200 km depth and the two planes are separated by ~40 km [*Shiobara et al.*, 2005; *Wiens et al.*, 2005]. Convergence at the trench is in a direction of N80W at 4.5 cm a^{-1}, and the full spreading rate at the Mariana spreading center is ~2.6 cm a^{-1} [*Kato et al.*, 2003]. The Mariana trench is slowly advancing in the hot spot reference frame (moving in the westward direction) and plate motions suggest that back-arc deformation is primarily controlled by Philippine Sea Plate motions [*Heuret and Lallemand*, 2005; *Scholz and Campos*, 1995].

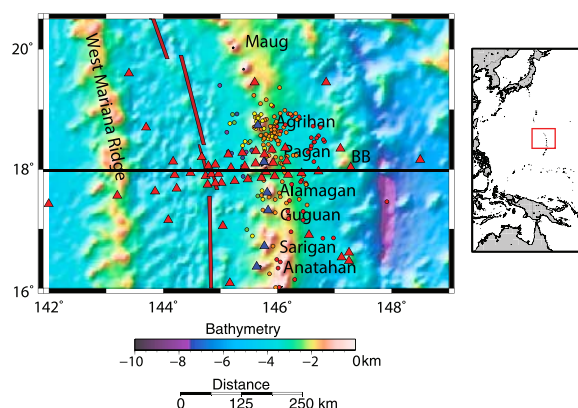[8] In addition to tectonic observations, geochemical variations have been observed across and

Figure 1. (right) Location and (left) bathymetric station map of the Mariana subduction system. Thick black line shows the cross section used in tomographic image. Land stations are denoted by blue triangles, and OBS stations are denoted by red triangles. Only stations returning data used in the attenuation study are shown. Earthquakes used in this study are plotted as small circles and color-coded as a function of depth: red <100 km, orange 101–200 km, yellow 201–300 km, green 301–400 km, blue 401–500 km, and violet >501 km. Thick red line sketches the back-arc spreading center.

along the arc [*Kelley et al.*, 2003; *Pearce et al.*, 2005; *Shaw et al.*, 2008]. Studies of the Mariana back arc show some subduction component [*Pearce et al.*, 2005], the distribution and inferred depth extent of which could help place constraints on melt and/or fluid pathways. The mantle source of the back-arc basin basalts is known to contain a large amount of water (~0.01–0.37 wt% H_2O) compared to other back-arc mantle sources, perhaps exceeding the nominal storage capacity of olivine [*Kelley et al.*, 2006]. On that basis of the spatial distribution of high and low Nb/Yb concentrations, several loci of mantle upwelling may exist beneath the Mariana spreading center [*Pearce et al.*, 2005], whereas analogous studies at other back-arc spreading centers suggests that mantle flows in one dominant direction [*Pearce and Stern*, 2006].

[9] Prior seismic studies in the Mariana arc system suggest that the back-arc spreading center is characterized by *S* wave velocities that are unusually fast (~4.15 km s^{-1}) compared to other back-arc spreading centers [*Wiens et al.*, 2006]. This observation is consistent with bathymetric and petrologic indications that the upper mantle is relatively cool (1350°C potential temperature) for a back-arc spreading center [*Kelley et al.*, 2006].

2.2. Seismic Attenuation

[10] Seismic attenuation, or the fractional loss of energy per wave cycle, is characterized by the quality factor (Q) [Knopoff, 1964] where the amplitude of seismic wave (A) is

$$A \sim e^{-\pi f \tau \frac{1}{Q}} = e^{-\pi f t^*} \tag{1}$$

where f is frequency, τ is the traveltime of the raypath, and letting $t^* = \tau/Q$ simplifies the expression (see Der [1998] and Jackson [2007] for reviews of seismic attenuation and physical mechanisms). Laboratory experiments at seismic frequencies show that seismic attenuation (Q^{-1}) increases with temperature following the high-temperature background formalism of

$$Q^{-1} \sim \left[\omega e^{-\frac{E}{RT}}\right]^{\alpha} \tag{2}$$

where ω is angular frequency, E is the activation energy, R is the universal gas constant, T is temperature, and α is the frequency-dependent exponent (approximately 0.27 for mantle materials where thermal relaxation is the dominant attenuation mechanism [Jackson et al., 1992, 2002]).

[11] In general, seismic attenuation results from intragranular (movements of point defects and dislocations) and intergranular (grain boundary migration or grain boundary sliding) processes (for a review, see Jackson [2007]). In addition, recent advances in laboratory experiments show that water and melt have significant effects on seismic attenuation. The overall effect of melt is to reduce the frequency dependence, such that α will be small or close to zero [Faul et al., 2004], whereas experimental results on the effects of water show that attenuation increases with water content [Aizawa et al., 2008].

2.3. Seismic Attenuation Structure of Subduction Zones: Previous Work

[12] Seismic attenuation using data from local earthquakes has been studied in many subduction zones, most notably in Tonga-Fiji [Bowman, 1988; Roth et al., 1999; Wiens et al., 2008], the Alaska Range [Stachnik et al., 2004], Costa Rica and Nicaragua [Rychert et al., 2008], New Zealand [e.g., Eberhart-Phillips and Chadwick, 2002], Europe [e.g., Goes et al., 2000], the northern Philippine Sea [e.g., Shito and Shibutan, 2003a, 2003b], Japan [e.g., Tsumura et al., 2000], and the Central Andes [Schurr et al., 2003]. Overall, these

studies show that the typical depth extent of a high Q^{-1} region beneath an island arc is ~100 km depth, but has been observed as shallow as ~50 km. High Q^{-1} anomalies beneath back-arc regions can persist to 150 or <200 km depth and they appear to extend in broad swaths away from the trench. The Alaska Range, which lacks active arc volcanism, shows much lower attenuation than other active arcs [Stachnik et al., 2004], whereas the Tonga mantle wedge with both active arc and spreading center magmatism, shows higher attenuation than other regions [Roth et al., 1999; Wiens et al., 2008]. Aside from teleseismic studies showing high attenuation in the Mariana back arc (with long wavelength resolution) [Barazangi et al., 1975; Warren and Shearer, 2002], seismic attenuation has not been investigated in the Mariana subduction system.

[13] Few studies have imaged attenuation structure at mantle depths beneath spreading centers. One study comparing teleseismic surface wave phase velocity and attenuation results beneath the fast spreading East Pacific Rise suggests the presence of melt and/or water beneath the ridge (the MELT region [Yang et al., 2007]). However, as far as we know, the only back-arc spreading center that has been imaged for a high-resolution seismic attenuation study is the fast spreading Lau system [Roth et al., 1999; Wiens et al., 2008]. To the best of our knowledge, this is the first study of seismic attenuation at mantle depths beneath a slow spreading ridge.

3. Data and Methods

3.1. Data Collection and Selection

[14] This study uses seismic data from the 2003–2004 Multiscale Seismic Imaging Experiment in the Mariana Subduction System, which was a deployment of 20 land broadband seismographs and 58 semibroadband OBSs extending from May 2003 to May 2004. The land stations used Streckheisen STS-2 and Guralp CMG-40T sensors and were deployed on each island between Guam and Agrihan. The 58 OBSs surround the deepest earthquake locations near Pagan Island and traverse the trench, fore arc, island arc, and back-arc spreading center, extending across the West Mariana Ridge (Figure 1). Fifty OBSs used three-component Mark Products L4 sensors with 1 Hz natural period and modified amplifiers to extend long-period performance and were operated by Lamont Doherty Earth Observatory. The remaining eight OBSs used
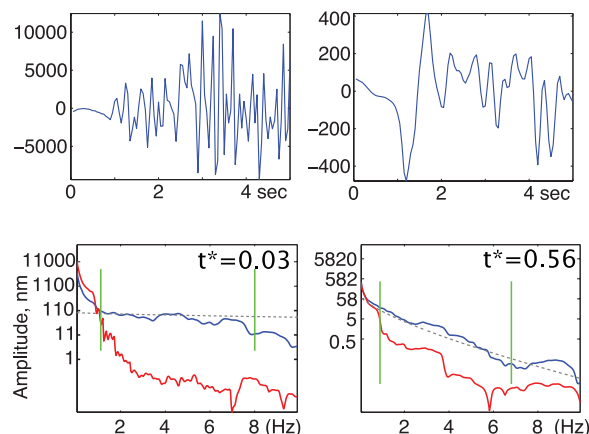
Figure 2. Example *P* wave spectra for a (left) fore arc OBS and (right) spreading center OBS from an earthquake located at 18.8°N, 145.7°E and 213 km depth on 8 August 2003 at 1117:48 UTC. (top) Waveform and (bottom) corresponding amplitude spectra showing signal spectra (blue) and noise spectra taken from time period immediately prior to the arrival (red). Grey dashed lines show the best fitting spectral solution. Green lines show spectral limits used in the source parameter and *t** inversion.

Precision Measuring Devices (PMD) sensors and were built by H. Shiobara at the University of Tokyo [*Shiobara and Kanazawa*, 2008]. The data set is limited to some extent by instrumentation problems: 35 new U.S. OBSs stopped recording data ~50 days after deployment because of a firmware error, and 8 U.S. OBSs were not recovered. Nonetheless, usable data were returned by 70 stations, and 41 instruments returned data for the entire planned deployment. A table of station locations and further details are given elsewhere [*Pozgay et al.*, 2007].

[15] We select local earthquakes from the U.S. National Earthquake Information Center (NEIC) catalog, in addition to smaller earthquakes that are only detected by our local temporary broadband network. We use earthquakes between 16°–19°N with more than 20 arrival time picks to ensure accurate source parameter determination. To eliminate complex ray propagation effects typically found for shallow paths, we require earthquake depths to be greater than 35 km. All earthquakes are relocated with the linearized least squares *dbgenloc* earthquake location module within the Antelope database software program [*Quinlan*, 1995]. After removal of several poorly recorded events, the final data set consists of 189 local earthquakes.

3.2. Determining *t** Values and Source Parameters

[16] We use a path-averaged method to solve for the attenuation parameter *t** for each *P* and *S* phase. For each earthquake (*k*) recorded at each station (*j*), we invert the observed seismic spectra for a single corner frequency (f_{ck}) and seismic moment (M_{0k}) for the event and the spectral decay attenuation parameter (t_{jk}^*) for the path to each station. Emphasizing improvements, we present the method here and refer the reader to comprehensive descriptions elsewhere [*Stachnik*, 2002; *Stachnik et al.*, 2004].

[17] We assume that the displacement spectrum can be represented by

$$A_{jk}(f_i) = \frac{C_{jk} M_{0k} e^{-\pi f_i t_{jk}^*}}{1 + (f_i + f_{ck})^2} \qquad (3)$$

[e.g., *Anderson and Hough*, 1984], where C_{jk} accounts for frequency-independent effects, f_i is the *i*th frequency, and t_{jk}^* is the frequency-dependent attenuation factor $t^* = t_0^* f^{-\alpha}$, where t_0^* is the attenuation factor at 1 Hz and α is the frequency-dependent exponent. If attenuation is due to thermal effects, laboratory experiments show that α is approximately 0.27 [*Jackson et al.*, 2002, 2006]. For each waveform, we remove the instrument response, data mean, and trend; we compute corrections for geometric spreading [*Kanamori and Stewart*, 1976] and free surface effects [*Helmberger*, 1974]; and we apply a spherically averaged radiation pattern correction [*Aki and Richards*, 2002]. The latter three corrections make up the frequency-independent C_{jk} term.

[18] In practice, we remove noise outside the frequency band of interest by applying a band-pass filter to each waveform (0.05–10 Hz) and then window each arrival with a 5 s window starting 0.5 s before the arrival pick, with the noise window of same length immediately preceding the signal window on the same channel. We use the vertical channel for the *P* arrival and the transverse component for the *S* arrival at island stations. For OBS stations, we use the horizontal channel with the largest amplitude *S* arrival. For each station, we compute the spectra using the multitaper spectral analysis method (Figure 2) [*Park et al.*, 1987; *Thomson*, 1982]. We interactively pick each spectral frequency band over which to compute *t** while ensuring that the usable frequencies are within the filtered passband and that the signal is well above

the noise level determined from the spectra of the window preceding the phase (Figure 2).

[19] We use nonnegative least squares to solve a linearized form of equation (3) for t_{jk}^*, M_{0k}, and f_{ck}. The nonlinear part is solved by a grid search over f_{ck}. Since there is a tradeoff between f_{ck} and t^* [*Anderson*, 1986] that sometimes gives unreasonable values of f_{ck}, we use a priori information to restrict the range of allowable corner frequencies to follow acceptable moment–f_c relations. In order to adopt this restriction, we require information about the earthquake size, which we have in the form of local magnitudes (M_L) as determined by the *dbgenloc* earthquake location regime [*Quinlan*, 1995]. We assume that a reasonable corner frequency should approximately follow [*Anderson*, 1986]

$$f_{ck} = 0.49\beta\left[\frac{\Delta\sigma}{M_0}\right]^{1/3} \qquad (4)$$

where β is the shear velocity (assumed 4 km/s) and $\Delta\sigma$ is stress drop, and we employ the relation

$$\log(M_0) = 1.5M_L + 16 \qquad (5)$$

to obtain an approximate M_0 from M_L [*Hough*, 1996; *Hough et al.*, 1999]. We use this relation only to obtain approximate f_{ck} ranges over which to perform the grid search for f_{ck} and other parameters determined in the nonlinear part of the problem. We assume that $\Delta\sigma$ is within a broadly expected range of 1–1000 bars and, in this way, compute lower and upper limits for f_{ck} that allow for variations in event $\Delta\sigma$, as well as uncertainties in M_L and β. Subsequently, we require that the upper and lower bounds of the allowable f_{ck} range be within the minimum and maximum frequency bands used for each earthquake (i.e., the band-pass filter 0.05–10 Hz). Using these limits for f_{ck}, we loop over f_{ck} with increments of 0.05 Hz for values below 1 Hz and 0.1 Hz for higher frequencies and solve for the best seismic moment and attenuation operator at each corner frequency. P and S can be analyzed separately, resulting in a solution that consists of a corner frequency ($f_{ck(P,S)}$) and seismic moment ($M_{0k(P,S)}$) for each event and wave type (P or S) and a $t_{jk(P,S)}^*$ value for each observed waveform. In some cases we require that the S wave corner frequency, which is typically less well constrained, to be equal to $f_{c(P)}$ divided by 1.5, as expected for circular ruptures [*Madariaga*, 1976].

[20] For an example earthquake with 23 P arrivals and 12 S arrivals, *dbgenloc* calculated $M_L = 4.25$

during the earthquake relocation process, such that we estimate M_W as 4.30 from equation (5) and f_{ck} will be constrained to be within the range 0.63–6.3 Hz. Thus, we do a grid search with f_{ck} ranging between 0.63 and 6.3 Hz. The optimal solution corresponding to the minimum misfit provides us with an $f_{ck(P)} = 1.8$ Hz and an $M_{0(P)} = 4.35$. This earthquake is reported in the U.S. National Earthquake Information Center database with $m_b = 4.4$, which agrees quite well.

[21] In order to investigate the effects of frequency dependence and source parameter assumptions, we repeat the t_{jk}^* determination procedure using a variety of assumptions (Table 1). We investigate different values of the frequency-dependent exponent α (0.0, 0.1, 0.27, and 0.6) and invert for $f_{c(P)}$, $M_{0(P)}$, and $M_{0(S)}$ at each α (cases 1–4 in Table 1). We also investigate in case 5 the effect of corner frequency variations by inverting for all t_{jk}^* estimates (at $\alpha = 0.27$) assuming a corner frequency given by equation (4) and a constant stress drop of 30 bars (3 MPa) (the interplate earthquake average [*Kanamori and Anderson*, 1975]). We investigate source parameter assumptions by imposing several restrictions: in case 6, we let $f_{c(S)} = f_{c(P)}$; in case 7, $M_{0(S)} = M_{0(P)}$, $f_{c(P)} = 1.5*f_{c(S)}$; in case 8, $M_{0(S)} = M_{0(P)}$, $f_{c(S)} = f_{c(P)}$, and $\alpha = 0$; and case 9 is the same as case 8 but $\alpha = 0.27$. Cases 8–9 are computed for comparison to results from spectral ratio methods, which assume that source parameters are equal for P and S [e.g., *Roth et al.*, 1999]. With the restriction of $M_{0(S)} = M_{0(P)}$, we ensure that the S wave moment and corner frequency are compatible with the P wave parameters and we can use S information from events with a smaller number of S arrivals.

[22] After reviewing the results of the different assumptions (Table 1), we chose to use the assumption that $M_{0(P)} = M_{0(S)}$, require that $f_{c(P)}$ should exceed $f_{c(S)}$ by 1.5, and assume the experimentally determined $\alpha = 0.27$ (case 7). These assumptions appear well justified theoretically and help increase the data set of useable waveforms, since many events do not have enough good S waveforms to independently determine the moment and corner frequency reliably. In addition, determining the optimal α on the basis of our data set alone yielded large uncertainties, so it seemed prudent to use the experimentally determined value.

3.3. Results and Error Estimates for t^*, f_c, and M_0

[23] For the 189 earthquakes analyzed, the final data set contains 2438 t_P^* and 439 t_S^* estimates

Table 1. Median t^* Results

Case	α	Note	Fore Arc[a] t^*_P	t^*_S	Arc t^*_P	t^*_S	Back Arc t^*_P	t^*_S	All t^*_P	t^*_S	N_P[b]	N_S[b]
1	0	$f_{c(P)} = 1.5*f_{c(S)}$	0.07	0.14	0.09	0.20	0.14	0.28	0.10 ± 0.004[c]	0.20 ± 0.011	2151	350
2	0.1	$f_{c(P)} = 1.5*f_{c(S)}$	0.08	0.17	0.12	0.24	0.17	0.32	0.13 ± 0.005	0.25 ± 0.012	2227	360
3	0.27	$f_{c(P)} = 1.5*f_{c(S)}$	0.14	0.23	0.17	0.33	0.25	0.42	0.19 ± 0.007	0.33 ± 0.016	2317	372
4	0.6	$f_{c(P)} = 1.5*f_{c(S)}$	0.39	0.65	0.41	0.68	0.58	0.81	0.45 ± 0.016	0.69 ± 0.03	2423	413
5	0.27	fixed $f_{c(P)}$, $f_{c(P)} = 1.5*f_{c(S)}$	0.18	0.31	0.21	0.34	0.30	0.49	0.23 ± 0.007	0.36 ± 0.016	2389	386
6	0.27	$f_{c(P)} = f_{c(S)}$	0.14	0.29	0.17	0.36	0.25	0.47	0.19 ± 0.007	0.37 ± 0.016	2309	388
7	0.27	$f_{c(P)} = 1.5*f_{c(S)}$, $M_{0(s)} = M_{0(P)}$	0.14	0.34	0.17	0.42	0.25	0.53	0.19 ± 0.007	0.43 ± 0.017	2438	439
8	0	$f_{c(P)} = f_{c(S)}$, $M_{0(s)} = M_{0(P)}$	0.07	0.20	0.09	0.26	0.14	0.38	0.10 ± 0.004	0.27 ± 0.011	2258	408
9	0.27	$f_{c(P)} = f_{c(S)}$, $M_{0(s)} = M_{0(P)}$	0.14	0.34	0.17	0.42	0.25	0.53	0.19 ± 0.007	0.43 ± 0.017	2301	436

[a] Fore arc versus arc separation is at 146°, and arc versus back arc separation is at 145.5°.
[b] N_P and N_S are the number of P and S raypaths, respectively.
[c] Median errors are described in section 3.3.

(Figures 3 and 4 and Table 1). Mean values of the high and low spectral bands for P (S) are 7.9 ± 1.4 (4.7 ± 2.2) and 1.3 ± 0.8 (0.8 ± 0.7) Hz, respectively. As expected, t^* estimates are higher in the back arc than in the arc. Results for different values of α (Table 1) [see *Pozgay*, 2007] show that absolute t^* estimates increase with increasing α as would be expected [e.g., *Stachnik et al.*, 2004]. Following error estimation from standard linear inverse theory, we compute the L_2 norm of the residual in the spectral fit, the residual variance, and the formal error in t^* for each measurement (Figure 4) [*Menke*, 1984; see *Pozgay*, 2007]. Median t^*_P (t^*_S) values are 0.14 (0.34), 0.17 (0.42), and 0.25 (0.53) for raypaths dominantly traveling beneath the fore arc, the arc, and back arc, respectively.

[24] For large attenuation, corner frequencies determined by spectral analysis may be underestimated for earthquake magnitudes $M < 4$ [*Anderson*, 1986]. However, seismic moment magnitudes range from 2.6 to 5.0, show good agreement for both P and S, and are consistent with database M_L and, where possible, the NEIC M_b or Harvard CMT M_0 [see *Pozgay*, 2007]. As such, we believe that source parameter determination is well resolved. Further evidence of this is the similarity in results that assume the corner frequency of the source to the case with the same α and inverting for f_c [see *Pozgay*, 2007].

3.4. Trends in the Individual Data

[25] Using standard relations, we compute a path-averaged Q estimate for each t^* estimate by

$$t^*_q = \frac{\tau_q}{Q_q} \qquad (6)$$

where τ is the traveltime and the subscript q denotes the phase (either P or S). As expected, we observe higher average attenuation at stations near the back-arc spreading center than compared to fore-arc stations (Figure 3). There is, however, an interesting pattern in Q_P/Q_S ratios such that stations in the fore arc and near the spreading center have lower values than do arc stations (for a comprehensive discussion, see *Pozgay* [2007]). Overall, mean path-averaged Q_P/Q_S values for the entire data set vary with different source assumptions and different values of α, ranging from 0.8 to 2.1 with a mean of 1.44 ± 0.4.

3.5. Tomographic Inversion

[26] We use the final data set of ~2900 t^* estimates to invert for the two-dimensional Q^{-1} structure along a cross section at 17.95°N. We design our model with nodes spaced 25 km apart comprising a total space of 800 km in the horizontal direction and 650 km in the vertical direction. After *Conder and Wiens* [2006], we use a three-point pseudo-bending ray tracing method [*Um and Thurber*, 1987; *Zhao et al.*, 1992] to trace the rays through a P and S wave velocity model determined from the same Mariana data set [*Barklage et al.*, 2006]. Raypath hit count for both P and S clearly show excellent resolution throughout the mantle wedge, although few S waves are recorded beyond the back-arc spreading center because of high attenuation (Figure 5). Since we are inverting for mantle attenuation, nodes at the surface (z = 0) are penalized against an a priori Q_P value of 600, deviations in this value have little effect on the resulting mantle Q_P structure [see *Pozgay*, 2007].
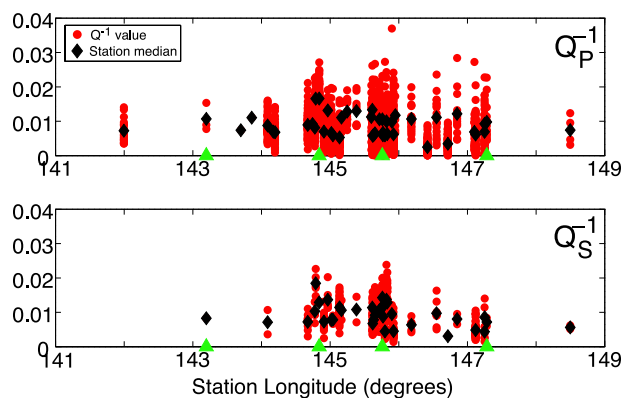
Figure 3. Attenuation results (case 7, Table 1) for (top) P and (bottom) S (red circles) plotted as the average attenuation along the path ($Q^{-1} = t*/\tau$, where τ is traveltime). Station medians (black diamonds) are plotted for each station at the corresponding station longitude. Green triangles show the location of the West Mariana Ridge, back-arc spreading center, island arc, and Big Blue Seamount in respective order from left to right.

Raypath lengths in the crust are assumed to have no contribution to the observed attenuation. We assume crustal thicknesses of 15 km beneath fore-arc stations, 20 km beneath arc stations, and 5 km beneath back-arc stations consistent with recent seismic refraction studies [after *Takahashi et al.*, 2007]. Inverse standard deviations of the t* estimates are used as the data weights.

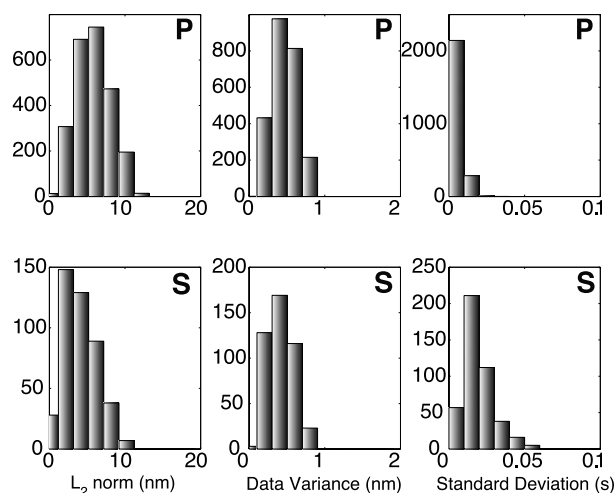[27] Second derivative smoothing constraints are implemented directly into the partial derivative

Figure 4. Histograms of individual t* error estimates for (top) P and (bottom) S showing (left) L_2 norm of residual and (middle) data variance of the spectral fit both in units of spectral displacement amplitude (nm) and (right) standard deviation of the t* estimates in units of s. See text section 3.3.

matrix [see *Conder and Wiens*, 2006; *Menke*, 1984]. To choose the optimal smoothing values, we inspect the data variances using the tomographic synthetic data test model A (see section 4.3) [see *Pozgay*, 2007, Appendix 3.A]. We select the value that best minimizes both the data variance and smoothing.

[28] The tomographic inversion equation is given by:

$$t_i^* = G_{ij}m_j = \sum_j \frac{l_{ij}}{V_j}\frac{1}{Q_j} \qquad (7)$$

where l is the path length for the ith ray in the jth block, V_j is the velocity in that block, and Q_j^{-1} is the desired attenuation model parameter for that block. We compute the kernel G_{ij} by tracing rays through the velocity model and invert for Q_j^{-1} using both singular value decomposition (SVD) and nonnegative least squares (NNLS), which show nearly identical results when >96% of the
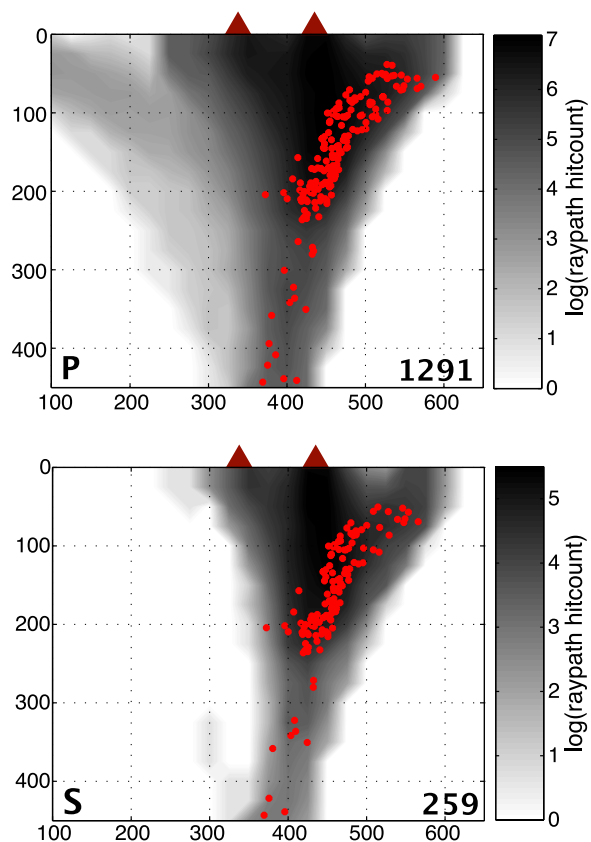

Figure 5. Cross sections showing the raypath hit count per node for (top) P and (bottom) S waves. The maximum hit count is printed in the bottom right corner of each panel. The node spacing is 25 km. Red dots are earthquake locations, and red triangles show the location of the spreading center (left triangle) and island arc (right triangle).
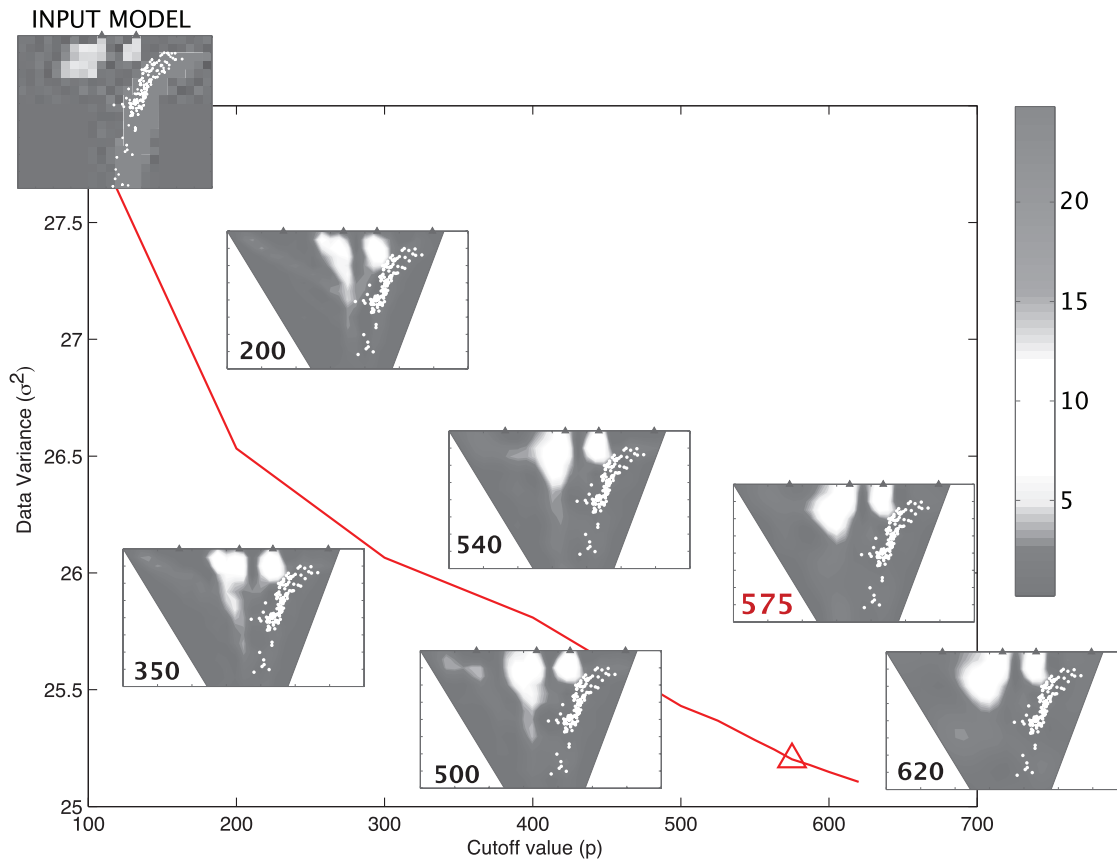
Figure 6. Data variance (σ^2) for different cutoff (p) values for SVD inversion. Q_P^{-1} solutions from the SVD inversion for synthetic data test model A (see section 4.3) are shown for reference. p value is printed in the bottom left corner of each panel.

singular values from the SVD inversion are used [see *Pozgay*, 2007]. However, the advantages of the SVD algorithm are apparent when reducing the number of singular values (p); the optimum p value in theory completely separates the constrained and unconstrained spaces. Using inversion results from a synthetic data test (model A, see section 4.3), we investigate data variances for different singular value allowances and choose p such that the resolution is maximum and data variance is minimum (Figure 6) [see *Pozgay*, 2007]. Lowering the p value has an overall effect of reducing the signal in poorly resolved parts of the model, but for p values less than ~550, important features are lost and the variance becomes much higher. We choose $p = 575$ with which to obtain our final results. Negative Q values in the SVD solution are only present in areas with very high Q values (low attenuation) in the NNLS solution, which are usually poorly resolved (see section 4.3). Furthermore, the similarity of SVD and NNLS results indicates that these few negative Q values do not significantly affect the rest of the derived model or the fit to the data.

[29] Since we have a small number of S data, we wish to employ a joint inversion so that P data helps constrain the S attenuation structure. We thus parameterize the solution using Q_P^{-1} and Q_P/Q_S and employ a piecewise joint inversion:

$$[t_P^*] = \left[\frac{l_P}{V_P}\right][Q_P^{-1}]$$

$$[t_S^*] = \left[\frac{l_S}{V_S}Q_P^{-1}\right]\left[\frac{Q_P}{Q_S}\right] \qquad (8)$$

where we omit the i and j subscripts for simplicity and show only the phase as subscript. We first solve the upper equation for Q_P^{-1} and then use those model parameters in the G matrix of the lower equation to solve for the Q_P/Q_S model parameters, which enables us to then calculate the Q_S structure.

4. Results

4.1. Tomography Results

[30] Tomographic images from the joint Q_P^{-1} and Q_P/Q_S SVD inversion (using data from our pre-
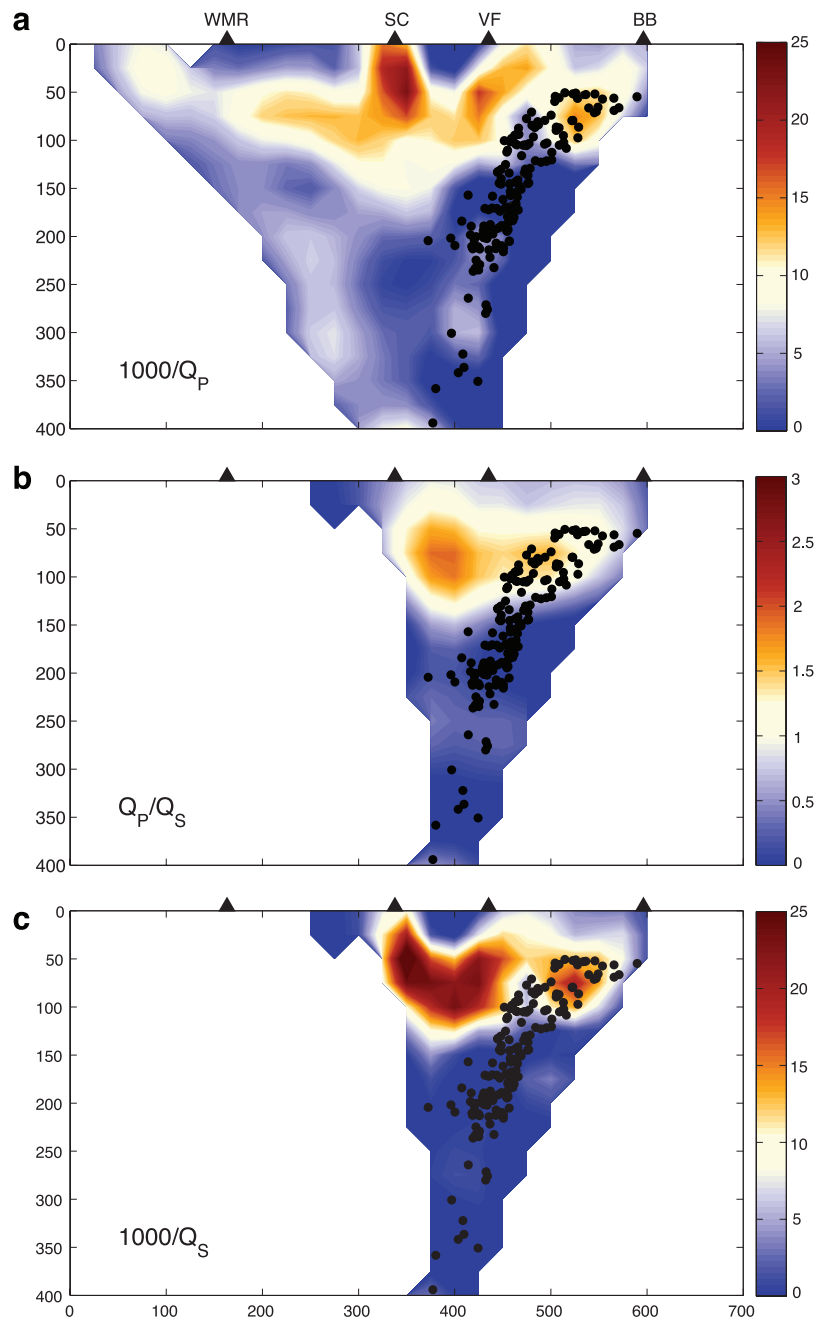
Figure 7.   (a) *P* wave, (b) Q_P/Q_S, and (c) *S* wave attenuation structures from the SVD inversion projected along the east-west line shown in Figure 1. Only nodes that have crossing rays are shown (see Figure 5). Circles are earthquakes, and triangles across the top from left to right correspond to the West Mariana Ridge (WMR), spreading center (SC), volcanic front (VF), and Big Blue Seamount (BB) (refer to Figure 1).

ferred data set, case 7) and subsequent Q_S^{-1} calculation clearly show the main features of the subduction zone, namely the low-attenuation subducting Pacific Plate and the higher-attenuation regions beneath the active volcanic arc and back-arc spreading center (Figure 7). The Q_P/Q_S inversion (Figure 7b) shows values approaching two in the core of the wedge, with lower values observed

everywhere else. Since the *P* and *S* wave tomography results are grossly similar (albeit the latter with reduced spatial resolution), we discuss the attenuation results in general and note specifically any deviations between the *P* and *S* structures.

[31]   The most prominent features of the images are high-attenuation regions beneath the Mariana volcanic arc and back-arc spreading center. The vol-
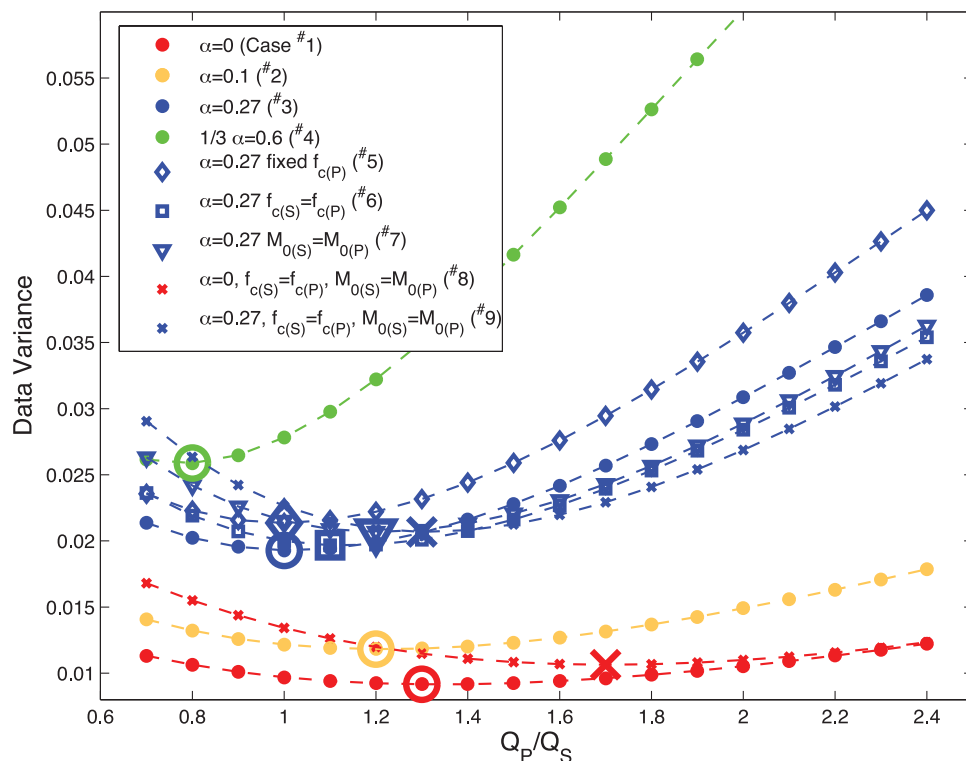
Figure 8. Q_P/Q_S versus data variance for each case in Table 1. Red symbols represent $\alpha = 0$, orange symbols represent $\alpha = 0.1$, blue symbols represent $\alpha = 0.27$, and green symbols represent $\alpha = 0.6$. Circles represent cases $1-4$ (Table 1); crosses represent cases $8-9$. Other symbols are as shown in the legend. Note that data variance for case 4 (green circles) has been scaled to fit on the current axes. Case numbers corresponding to Table 1 are in parentheses at the end of each legend entry.

canic arc anomaly extends from about $40-100$ km depth, terminating near the slab-wedge interface. It shows a minimum Q_P of about $56-70$ and Q_S of $45-58$ at a depth of 50 km. The anomaly beneath the back-arc spreading center forms a 75 km wide columnar feature in the Q_P image that extends from the Moho to about 100 km depth. Maximum attenuation is found at depths of $25-75$ km ($Q_P \sim 43-60$, $Q_S \sim 33-42$). The entire wedge region shows moderately high attenuation ($Q_P \sim 80-110$) at depths of around $75-100$ km. This high-attenuation region seems to form a link between the volcanic arc and the back-arc spreading center anomalies, which are well separated at depths less than 50 km by a prominent low-attenuation region.

[32] The core of the slab shows very low attenuation at depths greater than 100 km; however, there is a pocket of high attenuation within the slab at about 75 km depth ($Q_P \sim 66-79$; $Q_S \sim 50-73$). The shallowest region in the fore arc generally shows lower attenuation ($Q_P \sim 156-190$), but higher attenuation is observed beneath the serpentinite seamount ($Q_P \sim 100-103$) and immediately on the fore-arc side of the volcanic arc ($Q_P \sim 72-95$).

Since we have three OBSs surrounding Celestial Seamount (further south along the arc from the main OBS line), this seamount attenuation feature probably extends for some distance along strike. These fore-arc anomalies may be connected to the high-attenuation region at 75 km depth in the slab.

4.2. Average Q_P/Q_S Ratio

[33] Our preferred inversion method solves for the Q_P/Q_S ratio directly because we find that, when determined by conventional methods, this quantity varies with differing source parameter assumptions. However, for comparison with previous studies, we invert for Q_P^{-1} using t_P^* and t_S^* data for the different data sets given in Table 1 assuming fixed Q_P/Q_S ratios ranging from 0.7 to 2.5. The lowest data variance for each case is representative of the best fitting Q_P/Q_S ratio for that data set (Figure 8). We find that the best fitting Q_P/Q_S ratio increases with decreasing α (large open circles in Figure 8) and that the absolute minimum data variance occurs for $\alpha = 0$ (red symbols). Upon further scrutiny, one notices that for a given α (compare like colors in Figure 8), both the data
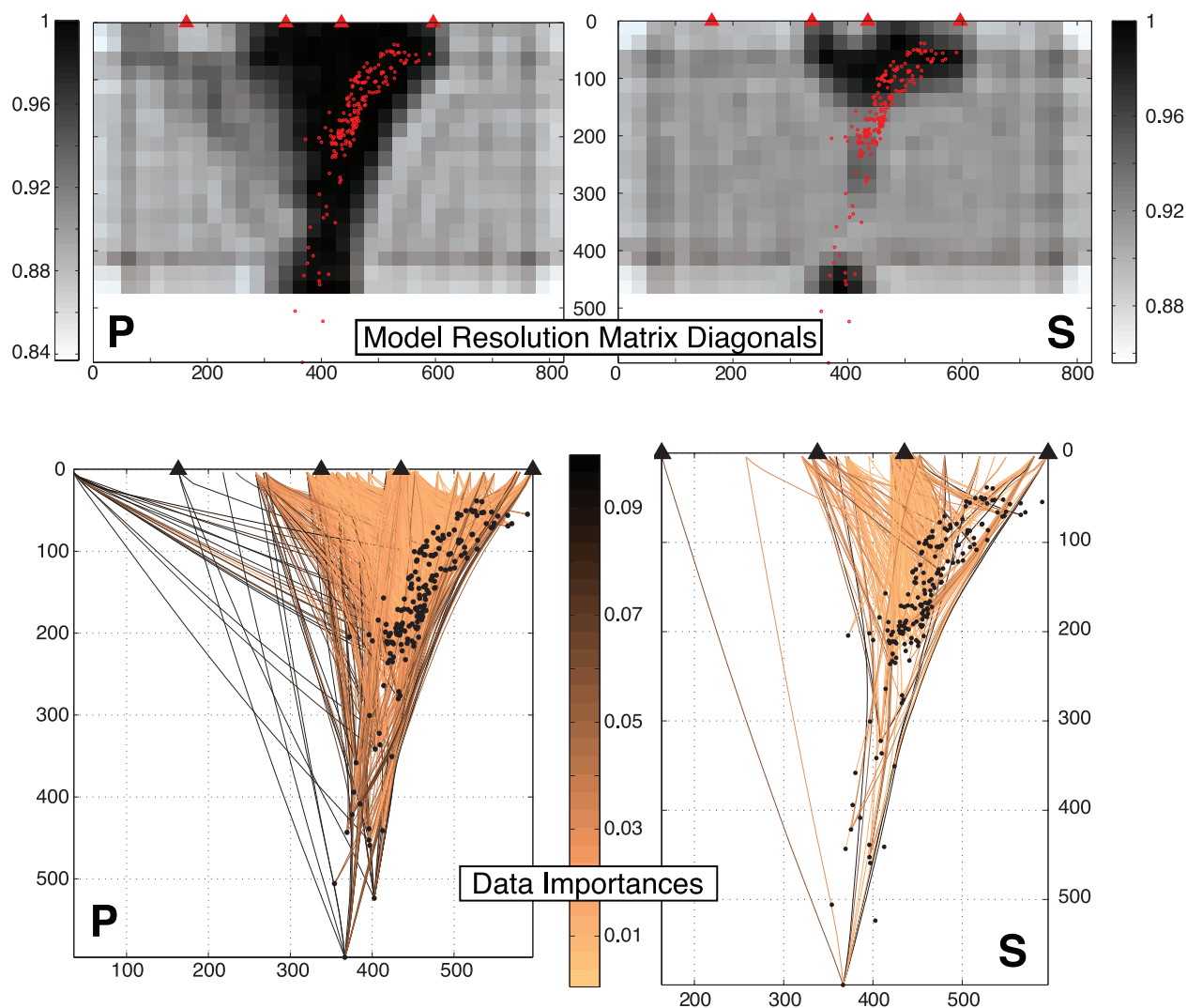
Figure 9. Model resolution matrix diagonals elements for each node for (top left) the *P* wave solution and (top right) the *S* wave solution showing how resolution varies within the attenuation images. Values close to unity indicate a well-resolved model parameter. (bottom) Raypaths color-coded by data importance. Color scale has been truncated to highlight the relatively important raypaths. Triangles across the top from left to right correspond to the West Mariana Ridge, spreading center, volcanic front, and Big Blue Seamount (refer to Figure 1).

variance and the Q_P/Q_S ratio increase with the degree of source similarity (equal f_c's or M_0's) between *P* and *S*.

[34] For our preferred data set (case 7 in Table 1), the best fitting Q_P/Q_S ratio is 1.2. This is significantly lower than theoretical estimates assuming zero attenuation in bulk ($Q_P/Q_S = 2.25$). These low values are not altogether unexpected, since the Q_P/Q_S tomography image (Figure 7b) shows that low Q_P/Q_S values predominate in many regions of the model.

4.3. Resolution Tests

[35] The output from a standard SVD inversion provides a comprehensive description of the model and data spaces. Model resolution matrix diagonal elements provide a measure of the resolution of each model parameter and show that we have excellent resolution within the slab, wedge, and beyond the spreading axis (Figure 9, top). Although smoothing is included in the model resolution matrix calculation and thus regions without raypaths have nonzero resolution, the region with high raypath hit count (Figure 5) shows values significantly higher than model parameters with low hit count and serves as a measure of which model parameters to mask from the images. A measure of the independence of each datum (raypath, or t^* estimate) is determined by the data importances, which show the expected result
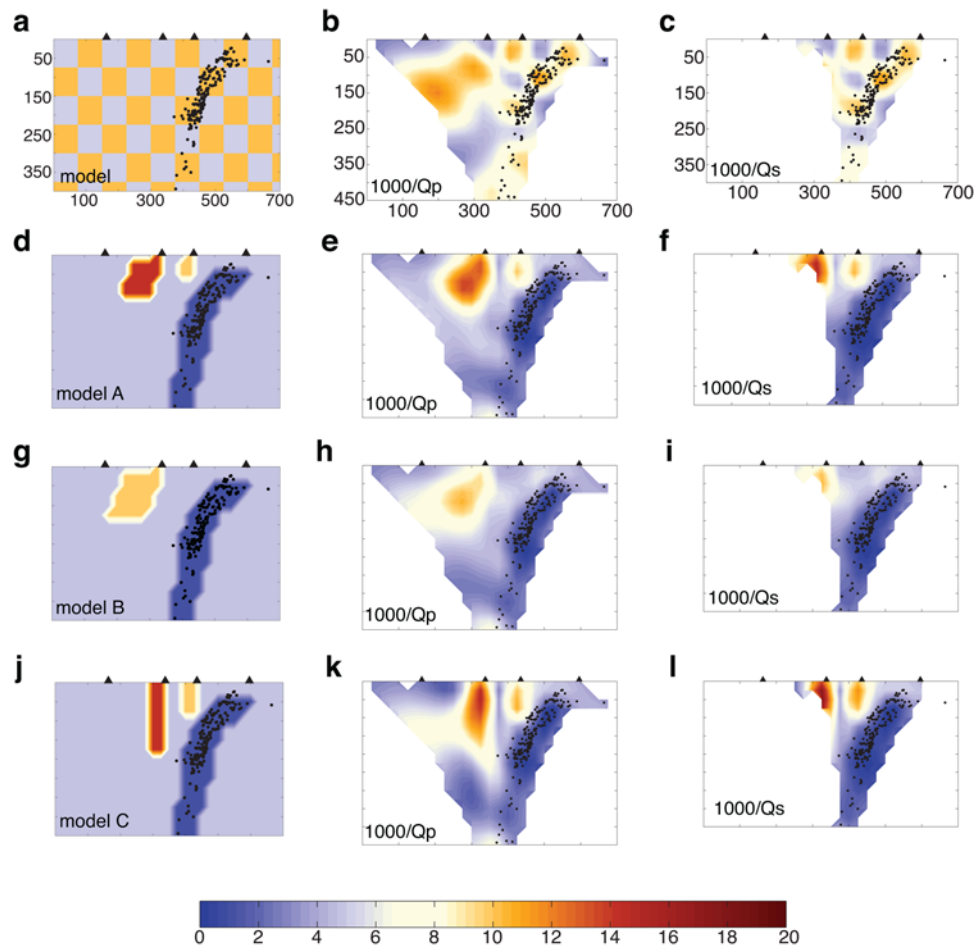
Figure 10. (a, d, g, j) Input models and resulting (b, e, h, k) *P* and (c, f, i, l) *S* output structures from tests with synthetic data. Input checkerboard model with alternating blocks of $Q = 200$ and $Q = 100$ (Figure 10a), model A with arc ($Q = 100$) and back-arc anomalies ($Q = 70$) (Figure 10d), model B with only a back-arc anomaly ($Q = 100$) (Figure 10g), and model C with two columns ($Q_{arc} = 100$, $Q_{backarc} = 70$) (Figure 10j). See text for model details (section 4.3). For all panels, the input anomalies are Q_P anomalies for the *P* test and are Q_S anomalies for the *S* test. Triangles across the top from left to right correspond to the West Mariana Ridge, spreading center, volcanic front, and Big Blue Seamount; earthquakes delineate the slab (refer to Figure 1). Axes are marked in Figures 10a–10c.

that isolated raypaths have greater data importance (Figure 9, bottom).

[36] We also use checkerboard tests to investigate the resolvability of a known input structure to the actual earthquake-station geometry used in the inversion. The degree to which we obtain the original input structure after computation and inversion of synthetic data provides an additional measure of confidence of the tomographic inversion. We design an input structure with alternating *Q* values of 200 and 100 with 75 km blocks (Figure 10a). We calculate synthetic t^* values for the actual raypaths corresponding to our observed data, add normally distributed random noise with the same data variance as errors from our real data, and invert to obtain the checkerboard resolution images for *P* and *S*

(Figures 10b and 10c). As expected, the resulting checkerboard patterns and amplitudes are well matched by our synthetic inversion for cells with high raypath hit count and high model resolution matrix diagonals.

[37] We also invert synthetic data sets to investigate the resolvability of observed or expected structures (Figures 10d–10l). We create several input models, all of which we use a slab *Q* value of 1000 and background *Q* value of 200. For easy comparison, we do not use input models with different values of Q_P and Q_S, instead we use the same input *Q* values for both structures (i.e., perfect solution would resolve background amplitudes of $Q_P = 200$ and $Q_S = 200$). *Q* values for the arc and spreading center anomalies vary among the

models, in addition to their extent and distribution (Figures 10b, 10d, and 10j). Each model space is designed to show resolution of a particular input structure, as a means of testing the limits of the data.

[38] Model A tests a generic subduction zone input with separate regions of high attenuation beneath the arc ($Q = 100$) and beneath the back-arc spreading center ($Q = 70$) (Figures 10d–10f). These regions are asymmetrically distributed in accord with models of asymmetric back-arc upwelling due to mantle flow [*Conder et al.*, 2002]. Model B tests the resolvability of a large anomaly at the back arc ($Q = 100$) (Figures 10g–10i) and model C investigates two distinct columns of different length and attenuation value ($Q = 100$ beneath the arc and $Q = 70$ beneath the back arc) (Figures 10j–10l).

[39] Using the same procedure as in the synthetic tests above, overall inversion results show remarkable recovery of both the shape and relative amplitude of the *P* and *S* input structures, especially when considering we added noise to the synthetic data and kept the smoothing the same as in our inversion with real data. The two distinct input anomalies in model A (Figure 10d) are remarkably recovered in shape and relative amplitude (Figures 10e and 10f). Even with noise added to the synthetic data, the two anomalies remain separate and do not connect. For model B (Figures 10g–10i), the back-arc anomaly is not smeared into the arc region and for model C (Figures 10j–10l) the two separate columns remain distinct in shape and relative amplitude down to 200 km depth. In all three synthetic models, the anomalies are well recovered, especially with the separate resolution of the arc and back-arc regions (i.e., they do not smear together). This distinct separation in resolution holds for both *P* and *S*. The amplitudes recovered are somewhat less than the input amplitude, thus indicating that the tomograms from our real data can be considered as a lower bound.

5. Discussion

5.1. Physical Factors Controlling Attenuation

5.1.1. Temperature

[40] Laboratory experiments demonstrate that the attenuation of subsolidus mantle materials is strongly temperature-dependent through the "high-temperature background" effect [*Faul and Jackson*, 2005; *Jackson et al.*, 1992, 2002, 2008; *Sato et al.*, 1989]. To help determine whether the attenuation

variations observed in the Mariana mantle wedge could result from temperature variations alone, we use both the *Faul and Jackson* [2005] and *Jackson et al.* [2002] formalisms with 1 cm grain size to compute temperatures in the core of the mantle wedge island arc anomaly where $Q_S \sim 43–80$ and find estimated mantle temperatures ranging from 1363 to 1508°C and ~1550 to 1700°C, respectively. Not surprisingly, these temperatures are higher than petrologically estimated magmatic temperatures from the 2003 eruption of Anatahan Volcano (1050–1100°C) [*de Moor et al.*, 2005]. These temperatures are also higher than temperatures expected from thermal models [*Conder*, 2007] and for the source region of island arc volcanoes [e.g., *Peacock et al.*, 2005], so high in fact for the *Jackson et al.* [2002] formalism that a different composition magma should erupt. Furthermore, *Jackson et al.* [2009] show that calculations from both of the aforementioned formalisms provide only a lower bound on the actual temperatures, suggesting even higher temperatures to account for the observed attenuation from thermal effects alone.

[41] Temperatures inferred for regions beneath the back-arc spreading center are similarly much higher than expected from petrologic constraints. The Q_S tomographic images suggest Q_S of 33–42, giving estimated temperatures of 1515–1580°C (using the *Faul and Jackson* [2005] formalism). In contrast, the major element chemistry of back-arc basin basalts suggests a mantle potential temperature of 1354°C [*Kelley et al.*, 2006]. The temperatures calculated from attenuation are also much higher than temperatures from thermal models [e.g., *Conder*, 2007; *Conder et al.*, 2002], which are generally calibrated to mantle potential temperatures inferred from petrological constraints.

[42] In addition to the fact that these temperature estimates inferred from the attenuation results are a lower bound [*Jackson et al.*, 2009], the disparity between these temperatures and other constraints on the temperature structure suggests that attenuation mechanisms throughout much of the subduction system are not dominated by high-temperature background, as commonly assumed. The attenuation beneath the volcanic arc and the back-arc spreading center is too large to result from temperature affects alone. We now discuss other effects that may lead to high attenuation in the mantle wedge.

5.1.2. Hydration

[43] One possible explanation for the high temperatures calculated from the shear wave attenuation

structure is that increased attenuation might result from the effects of hydration. One preliminary laboratory study shows that olivine containing ~0.3 wt% H_2O distributed in accessory hydrous silicate phases can have significant effects on seismic attenuation [*Aizawa et al.*, 2008]. This may have important consequences for attenuation observed in the highly serpentinized fore arc; however, although it is the first laboratory study showing significant attenuation increase in the presence of water, it does not provide a means to quantitatively evaluate these effects on observed seismic attenuation.

[44] In the absence of experimental data directly relating water content with seismic attenuation, *Karato* [2003] estimated the effect of water distributed as hydrogen defects bound in anhydrous minerals on seismic attenuation using the results of rheological experiments. The water content of the mantle source region for Mariana back-arc basin basalts as been estimated at 0.17 ± 0.04 wt% H_2O [*Kelley et al.*, 2006; *Wiens et al.*, 2006]. With this hydration level, temperatures would be lowered by ~150–180°C [*Karato*, 2003, Figure 3], which may be a good estimate for lowering the scaled temperatures beneath the back arc. Beneath the volcanic arc where water contents are as high as 0.5–0.8 wt% H_2O [*Kelley et al.*, 2006], the scaled temperatures would be lower by ~200°C. However, this may not be an accurate estimate because these high water concentrations might exceed the water storage capacity of the upper mantle (~0.12–0.38 wt% H_2O at 3 GPa [*Hirschmann et al.*, 2005]); in this case, the *Karato* [2003] formalism would no longer be valid, but attenuation would probably be further enhanced by hydrous minerals in grain boundaries [e.g., *Aizawa et al.*, 2008]. Both of these lower temperature estimates beneath the arc and the back arc could then provide temperature estimates in approximate agreement with preliminary thermal modeling results [*Conder*, 2007]. Thus, the high-attenuation regions found in the mantle wedge may result largely or in part from the effects of excess water given off by the downgoing slab and incorporated in nominally anhydrous minerals.

5.1.3. Melt

[45] Although hydration is a plausible mechanism contributing to the attenuation signal beneath the arc, another possible explanation for the high attenuation in the mantle wedge is the effect of partial melt on seismic attenuation, which is difficult to quantify as quantitative relations have not yet been determined by laboratory studies. However,

one laboratory study determined that partial melt enhances attenuation in the seismic frequency band [*Faul et al.*, 2004], most likely through a grain boundary sliding mechanism. The attenuation effects are large, such that only a 1% melt porosity corresponds to nearly an order-of-magnitude increase in attenuation. This suggests that the high-attenuation regions found beneath the arc and the back-arc spreading center could result from modest (<1%) amounts of in situ melt within the melt producing regions of the mantle wedge.

[46] Another interesting result from *Faul et al.* [2004] is that attenuation due to melt can be characterized by a near-lack of frequency dependence (α~0), providing a possible diagnostic criterion to distinguish the effects of melt from other parameters. Table 1 shows that t^* errors are lower for $\alpha = 0$ as compared with equivalent t^* estimates for $\alpha > 0$ (compare cases 1 and 3 and 8 and 9). Additionally, we observe that the data set of t^* estimates with $\alpha = 0$ provide the lowest data variance for each Q_P/Q_S ratio and also the highest path-averaged Q_P/Q_S ratio compared to the other data sets (red symbols in Figure 8). This suggests that a large number of raypaths might not have frequency dependence concurrent with a solely thermal attenuation mechanism ($\alpha = 0.27$) and might be directly indicative of smaller overall frequency dependence and linked to the presence of partial melt in agreement with other studies [*Faul et al.*, 2004; *Shito et al.*, 2004].

[47] While *Faul et al.* [2004] report an increase in attenuation due to the effects of melt, a different study finds that melt at the grain scale will not significantly affect seismic attenuation [*Gribb and Cooper*, 2000]. However, the authors suggest that a fractal tree model of melt transport (i.e., via an intergranular network [*Hart*, 1993]) could produce the large attenuation observed in many Q_S studies. Further laboratory work is needed to distinguish between the various studies of the effects of melting mechanisms and melt transport on attenuation.

5.2. Q_P/Q_S and the Attenuation Mechanism

[48] If bulk attenuation (Q_κ^{-1}) is negligible (as is commonly assumed), shear wave attenuation in the mantle will be greater than P wave attenuation with $Q_P/Q_S = 2.2–2.6$. Q_P/Q_S ratios significantly smaller than 2.25 can indicate the presence of bulk attenuation or wave energy attenuation due to scattering (for a review, see *Jackson* [2007]). Our Q_P/Q_S inversion generally shows values less than 2

in most regions of the model, with values approaching 2 only in the center of the mantle wedge. In addition, inverting for the best fitting average Q_P/Q_S ratio gives a value of 1.2 for our preferred $\alpha = 0.27$, or 1.7 for our preferred $\alpha = 0$ case (Figure 8, cases 7 and 9).

[49] Nonnegligible Q_κ^{-1} has been observed in many places [*Butler et al.*, 1987; *Gudmundsson et al.*, 2004; *Schlotterbeck and Abers*, 2001; *Stachnik et al.*, 2004]. In fact, *Roth et al.* [1999] found that the best fitting Q_P/Q_S ratio in Tonga-Fiji is 1.75, which is nearly identical to our determination made using the same assumptions of similar P and S source spectra and $\alpha = 0$. Several mechanisms have been suggested that could produce significant Q_κ^{-1}, such as partial melt [*Vaišnys*, 1968] or elastic processes such as scattering [*Aki*, 1975; *Butler et al.*, 1987; *Stachnik et al.*, 2004]. The latter is generally strongly frequency-dependent ($\alpha \sim 0.5$) [e.g., *Budiansky et al.*, 1983]. As our results suggest that strong frequency dependence ($\alpha = 0.6$) is not likely here (compare cases 1 and 4, Figure 8 and Table 1), we can rule out scattering as the dominant attenuation mechanism throughout the arc system. However, as significant lithospheric Q_κ^{-1} is not uncommon in older lithospheric regions [*Butler et al.*, 1987; *Stachnik et al.*, 2004], the effect of scattering probably plays a large role for attenuation measurements of raypaths traveling predominantly through the subducting old Pacific slab.

[50] Observed Q_P/Q_S values in other subduction zones range from 1.75 (Tonga/Lau [*Roth et al.*, 1999]) to 2.15 (Philippine Sea [*Shito and Shibutan*, 2003a]), both of which have shallow, poorly defined misfit minima suggesting large uncertainty (as does our result, Figure 8). In continental Alaska, path-averaged Q_P/Q_S values from raypaths through the mantle wedge are $\sim 1.2-1.4$ as compared to $\sim 1.0-1.1$ for slab paths [*Stachnik*, 2002] and further analysis showed a large effect of thick crustal material lowering the Q_P/Q_S ratio [*Stachnik et al.*, 2004]. Our preferred data set showed a minimum misfit for path-averaged Q_P/Q_S of 1.2 (case 7, Figure 8). However, for case 8 ($f_{c(P)} = f_{c(S)}$ and $\alpha = 0$, red crosses in Figure 8), the Q_P/Q_S ratio is 1.7, which is in excellent agreement with analogous frequency-independent spectral ratio Q^{-1} results from the Tonga/Lau system [*Roth et al.*, 1999]. Thus, our observation of significant bulk attenuation, as well as those in the literature, is well supported by the data, but the physical

mechanisms to produce such effects are still not well understood.

5.3. Attenuation Structure of the Subduction System

5.3.1. Fore Arc and Slab

[51] We image two high-attenuation regions in the Mariana fore-arc mantle wedge, one located at shallow depth just eastward of the volcanic arc and the other located near the Big Blue serpentinite seamount (Figure 7). This result is in sharp contrast to results from other subduction zones, which generally show very low attenuation in the fore-arc mantle wedge (see section 5.4). Raypath coverage shows several crossing rays within the high Q_P^{-1} region immediately east of the arc; however, the coverage is not optimal and might suggest that perhaps the depth extent of this region is not well constrained. If so, this region might correspond to a serpentinized low-velocity layer of nearly 30 km thickness extending to ~ 70 km depth as determined by receiver functions [*Tibi et al.*, 2008]. However, the depth extent of this region does agree with results from velocity tomography and magnetotellurics showing slow velocities and highly conductive anomalies at this depth [*Baba et al.*, 2004; *Barklage et al.*, 2006]. In addition, the horizontal location of this high-attenuation region corresponds to a possible intrusion locale ~ 15 km east of Pagan Island (A. Oakley, Sedimentary, volcanic and tectonic processes of the central Mariana arc: Part 1: Mariana Trough backarc basin formation and the West Mariana Ridge, submitted to *Geochemistry, Geophysics, Geosystems,* 2008), which could be indicative of widespread extension within the (near arc) fore arc in this region.

[52] A second high-attenuation anomaly ($Q_P \sim 100$) occurs directly beneath the active outer fore-arc serpentinite seamounts. Temperatures in the fore arc are expected to be cool, as suggested by thermal models and by low-T metamorphic rocks hat have been brought to the surface by serpentinite mud volcanism [*Fryer*, 1996]. The simplest explanation for the high-attenuation outer fore arc may be related to widespread extension and serpentization [e.g., *Fryer*, 1996; *Hyndman and Peacock*, 2003] induced by the release of fluids and sediment dehydration between $\sim 50-70$ km [*Rüpke et al.*, 2004]. Although there is very little experimental data investigating the effect of serpentine on seismic attenuation [e.g., *Kern et al.*, 1997] and attenuation studies have not been done yet in other

highly serpentinized fore arcs, the high-attenuation anomaly directly beneath the active fore-arc serpentinite seamounts is well supported by the raw data and we suggest that it is likely due to serpentine.

[53] The subducting slab shows high P and S attenuation at ∼50–100 km depth compared to the surrounding slab material. One interpretation for this anomalous region could be due to processes related to the release of fluids from the shallow slab. The anomaly resides within the ∼40-km-wide double seismic zone [*Wiens et al.*, 2005], where preliminary V_P/V_S results for the Marianas shows high values [*Barklage et al.*, 2006] and calculated temperature estimates (see section 5.1.1) are higher than the surrounding material. This could be indicative of partial hydration between the two seismic planes due to dehydration-related earthquakes within the lower plane [*Hacker et al.*, 2003; *Zhang et al.*, 2004]. This region has been observed in several other subduction zones at comparable depths and appears to correlate either with the double seismic zone [*Nakamura et al.*, 2006; this study] or with a zone of decreased seismicity [*Deshayes et al.*, 2007; *Rychert et al.*, 2008; *Stachnik et al.*, 2004] (see section 5.4).

5.3.2. Volcanic Arc

[54] We image a high Q^{-1} anomaly centered beneath the arc at a depth of about 50–100 km, and extending upward to the arc and the innermost fore arc. As water content in the mantle source beneath the arc is high [*Kelley et al.*, 2006] and theoretical and preliminary experimental studies suggest that water [*Aizawa et al.*, 2008] and melt [*Faul et al.*, 2004] can both have a large effect on seismic attenuation, it is likely that the observed attenuation anomalies are affected by water and/or melt (see section 5.2). This anomaly is almost certainly associated with the production of island arc volcanism and corresponds to high-attenuation and low-velocity anomalies observed beneath other arcs (see section 5.4). The subarc anomalies in other arcs, however, are sharply truncated beneath the volcanic front with low attenuation in the fore arc; whereas, in the Mariana arc the high-attenuation region extends into the fore arc, as do low-velocity anomalies in preliminary velocity tomography images [*Barklage et al.*, 2006].

[55] We can infer the degree to which the general shape and attenuation magnitude within the arc are recovered by our tomographic image based on comparison of forward modeling results (Figures 10d–10l) to the observed structures (Figure 7). The

forward models suggest that the attenuation magnitude and the location of the attenuation maxima are well recovered. Furthermore, they suggest that the high-attenuation region that connects the arc and back-arc anomaly at a depth of about 100 km is robust. Forward models did not produce such a connection unless one existed in the model used to produce the synthetic data (see additional models given by *Pozgay* [2007]). This suggests that the connection between the arc and back arc at ∼100 km depth is required by the data and likely is the locus for material transfer between the slab and back-arc region, as implied by the geochemical results that observe a slab signature from back-arc basalts [*Pearce and Stern*, 2006].

5.3.3. Back-Arc Spreading Center

[56] A pronounced ∼75 km wide columnar region of high attenuation exists directly beneath the spreading center at depths from 75 km to the surface. This feature is surrounded by low-attenuation regions at shallow depths (0–50 km) on both sides of the spreading axis and extends upward from the laterally extensive subhorizontal high-attenuation region that persists from the arc to beyond the back-arc spreading center, notably connecting the arc and back-arc anomalies at 75–100 km depth (Figure 7). This anomaly may have a sheet-like form aligned with the ridge axis in 3-D, as the data going into the tomographic inversion extend for some distance along-strike. One explanation for such high attenuation beneath the spreading center is a significant amount of partial melt (see section 5.2). Water is a less likely explanation, since the mantle source for the back-arc basalts contains less water than the mantle source for the arc volcanoes [*Kelley et al.*, 2006]. Attenuation beneath the back arc is higher than attenuation observed beneath the volcanic front, which may indicate that the back-arc region contains more in situ melt.

[57] Although there are only a few other studies of the attenuation structure of spreading centers, we note that the narrow, vertically elongated region of high attenuation here is in marked contrast to the broad attenuation anomaly beneath the fast spreading Lau back-arc spreading center [*Roth et al.*, 1999] (see section 5.4). The only attenuation study of a mid-ocean ridge shows no evidence of a narrow zone of high attenuation at the fast spreading East Pacific Rise [*Yang et al.*, 2007]. In addition to attenuation structures, upper mantle seismic velocity images can also provide important

constraints. Broad asymmetric low-velocity anomalies observed beneath fast spreading ridges in the Lau basin [e.g., *Conder and Wiens*, 2006; *Roth et al.*, 1999] and along the East Pacific Rise [*Dunn and Forsyth*, 2003; *Forsyth et al.*, 1998; *Hammond and Toomey*, 2003] also suggest a very broad melt production region beneath fast spreading centers. These observations are generally interpreted as indicating that the dynamics of fast spreading centers are dominated by passive mantle upwelling, with melt produced over a broad region and transported to the mid-ocean ridge [*Sparks and Parmentier*, 1991; *Spiegelman and McKenzie*, 1987]. In contrast, detailed seismic velocity images of slow spreading centers are very limited, with one study based on *PKP* traveltime delays suggesting a narrow low-velocity region beneath the mid-Atlantic ridge [*Forsyth*, 1996].

[58] We propose that the narrow zone of high attenuation imaged at the Mariana back-arc spreading center results from a narrow zone of enhanced melt production and high temperatures beneath the ridge. This implies that the mantle flow and melt production pattern near slow spreading ridges is fundamentally different from the broad melt production region beneath more well-studied fast spreading ridges. A narrow melt production region is consistent with models incorporating buoyant flow near the ridge crust [*Madge and Sparks*, 1997; *Su and Buck*, 1993], resulting in dynamic upwelling and melt production within a localized region that is less continuous along-axis. A more dynamic mantle melt production region is also consistent with significant along-axis variations in gravity and crustal thickness observed along the Mariana back-arc spreading center, with gravity lows representing the locations of dynamic mantle upwelling and thicker crust [*Kitada et al.*, 2006].

5.4. Comparison With Other Subduction Zones

[59] In order to compare our results with those from other subduction zones, we must account for different source parameter assumptions, different spectral frequency bands used, and different frequency-dependent exponents (α) because these different assumptions affect the resulting t^* values (and subsequently Q^{-1}) (see Figure 8 and Table 1). In this study, we find that assuming identical P and S source spectra ($f_{c(S)} = f_{c(P)}$) increases the resulting t^*_S values relative to the assumption where the corner frequencies are scaled by a factor of 1.5 (compare cases 3 and 6 and cases 7 and 9). Similarly,

$\alpha = 0$ yields lower t^* values and Q^{-1} compared to results assuming frequency-dependent attenuation.

[60] Previous studies suggest that seismic attenuation measurements are dominated by the attenuation near the upper limit of the frequency range [e.g., *Stachnik et al.*, 2004]. The use of an appropriate α should, in theory, allow measurements from different frequency ranges to be compared, but since direct determination of α from the seismic data is difficult, such comparisons are subject to some uncertainty. Thus, reliable comparisons should ensure that similar source assumptions (e.g., α value) and frequencies were used in each study. Different frequency ranges are noted to aid in this comparison (Table 2), however some studies have similar frequency ranges to this study (e.g., Costa Rica and Nicaragua [*Rychert et al.*, 2008]), so we can make direct comparisons there. We report our Q^{-1} results for $\alpha = 0$ and $\alpha = 0.27$ (Table 2) for direct comparison with these other studies with various assumed α values.

[61] Comparison of attenuation between different arcs (using the same frequency-dependent exponent) shows that northern Mariana Q_P^{-1} is among the highest attenuation measured in subduction zone mantle wedges, exceeded only by the Lau Basin region [*Roth et al.*, 1999; *Wiens et al.*, 2008]. The highest attenuation values for other subduction zones are generally focused in a small region directly beneath the arc volcanic front. However, much of the upper $\sim$100 km in Mariana shows a background $Q_P \sim 90-125$ (at $\alpha = 0$) with even higher attenuation localized directly beneath the volcanic front and beneath the back-arc spreading center. This background attenuation value represents higher attenuation than the maximum attenuation values reported from northern Honshu (at $\alpha = 0$, albeit at higher frequencies) [*Tsumura et al.*, 2000] and the amagmatic continental Alaskan arc (at $\alpha = 0$) [*Stachnik et al.*, 2004], which likely shows lower attenuation related to the lack of active volcanism. The background attenuation value in Mariana is comparable to the highest values observed in Costa Rica and Nicaragua, which are located directly beneath the arc front [*Rychert et al.*, 2008]. There is thus some suggestion that arcs with active back arcs have higher attenuation.

[62] The depth of maximum attenuation beneath the Mariana island arc ($\sim$75 km depth) is similar to that found at most other subduction systems such as Costa Rica and Nicaragua [*Rychert et al.*, 2008], continental Alaska [*Stachnik et al.*, 2004], Japan [*Takanami et al.*, 2000; *Tsumura et al.*, 2000], and

Table 2. Highest Q^{-1} Values in the Center of Mantle Wedge Anomalies[a]

Subduction Zone	Frequency (Hz)	Q_P	Q_S	Depth (km)	Citation
		$\alpha = 0$			
Northern Mariana (arc)	0.1–9.5	93–132	63–76	50–75	this study
Northern Mariana (back arc)	0.1–9.5	63–93	42–56	25–50	this study
Tonga-Lau (back arc)	0.1–3.5	47–60	–	50	*Wiens et al.* [2008]
Northern Honshu	1–20?	150–180	–	30–60[b]	*Tsumura et al.* [2000]
Southern Honshu	1–20?	150	–	80–100[b]	*Tsumura et al.* [2000]
NE Japan	1–8	–	70–120	55–90	*Takanami et al.* [2000]
Southern Bolivian Andes	1–7 or 1–30	80–150	–	85	*Schurr et al.* [2003]
Continental Alaska	1–19 (P), 0.3–9 (S)	537	283	75[b]	*Stachnik et al.* [2004]
Costa Rica	0.5–7	–	157–164	75[b]	*Rychert et al.* [2008]
Nicaragua	0.5–7	–	120–123	75[b]	*Rychert et al.* [2008]
		$\alpha = 0.27$			
Northern Mariana (arc)	0.1–9.5	56–70	45–58	50–75	this study
Northern Mariana (back arc)	0.1–9.5	43–60	33–42	25–50	this study
Continental Alaska	1–19 (P), 0.3–9 (S)	266	138	75[b]	*Stachnik et al.* [2004]
Costa Rica	0.5–7	–	84–88	75[b]	*Rychert et al.* [2008]
Nicaragua	0.5–7	–	76–78	75[b]	*Rychert et al.* [2008]

[a] Approximate value of maximum attenuation region in wedge core.
[b] Interpreted from figures in the original publication cited in column 6.

the Bolivian Andes [*Schurr et al.*, 2003]. The narrow band of high attenuation beneath the arc volcanic front in Mariana is similar in shape to the narrow island arc attenuation anomalies in Japan [*Tsumura et al.*, 2000].

[63] One major difference between results imaged here as compared to other subduction systems is the notable lack of a low-attenuation fore arc here. This transition is quite prominent in other subduction zones [*Rychert et al.*, 2008; *Schurr et al.*, 2003; *Stachnik et al.*, 2004]. As previously discussed (section 5.3.1), this may reflect the more widespread serpentinization of the Mariana fore arc relative to other fore-arc systems as evidenced by the nearby mud volcanoes. Future seismic experiments at other subduction zones with known serpentinized fore arcs (e.g., Cascadia) will help elucidate the effect of serpentinization.

5.5. Comparison With Lau

[64] The Tonga volcanic arc and Lau back-arc spreading center furnish a particularly interesting comparison with Mariana, since these two arcs are the only arc-back-arc systems for which we know the attenuation structure. Attenuation beneath the Central Lau Spreading Center (CLSC [*Roth et al.*, 1999; *Wiens et al.*, 2008]) is higher than in Mariana (Figure 11) when compared using similar source parameter assumptions and $\alpha = 0$. The maximum attenuation values of $Q_P \sim 63–93$ ($\alpha = 0$, case 8) are observed directly beneath the Mariana spreading center at $<\sim50$ km depth; in the CLSC, maximum

attenuation is $Q_P \sim 47–60$ and located between the arc and the spreading center at ~50 km depth. In both regions between the spreading center and extinct ridge (the West Mariana Ridge and the Lau Ridge), there is a shallow ($<\sim50$ km) low-attenuation region atop a swath of high attenuation extending asymmetrically from just west of each spreading axis to the western side of each extinct ridge.

[65] One main difference between the CLSC and Mariana is that the CLSC high-attenuation region extends to nearly 200 km depth along much of the profile, whereas in Mariana, the maximum depth extent is notably shallower ($\sim100–125$ km). This may result from the hotter mantle potential temperature beneath the Lau back arc inferred from seismic velocity and basalt geochemistry [*Wiens et al.*, 2006]. The warmer geotherm would result in deeper melting beneath the Lau basin [e.g., *Klein and Langmuir*, 1987]. Although major element melting is likely limited to depths less than 80 km even for the warmer mantle case [*Langmuir et al.*, 1992; *Shen and Forsyth*, 1995], very small component deeper melting may be facilitated by volatiles [*Dasgupta et al.*, 2007].

[66] The other major difference between CLSC and Mariana structures is that the CLSC high-attenuation region extends nearly across the entire Lau back-arc basin, over a width of about 200 km, whereas the Mariana high-attenuation region is limited to a 75-km-wide region immediately beneath the spreading center. Because of the instrument spacing, resolution in the Tonga-Lau study is limited
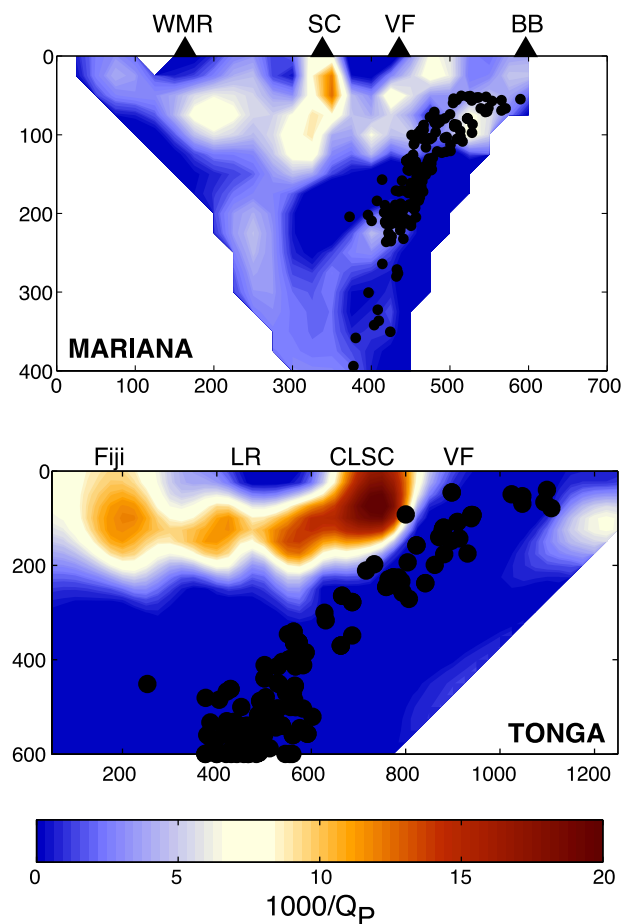
Figure 11. Q_P^{-1} tomography results with $\alpha = 0$ (case 8 in Table 1) for (top) Mariana compared with attenuation tomography results from (bottom) the Tonga/Lau system from the phase pair method. Abbreviations are West Mariana Ridge (WMR), spreading center (SC), volcanic front (VF), Big Blue Seamount (BB), Lau Ridge (LR), and Central Lau Spreading Center (CLSC). Lau basin results are directly from *Wiens et al.* [2008] but plotted with new color scale. Color scales of the two panels are equal and directly comparable.

compared to the Mariana study, thus limiting any details regarding the arc structure, but the wide high-attenuation region is clearly resolved. We interpret this difference as reflecting the difference between the passive mantle flow pattern found beneath fast spreading centers such as Lau and a narrow, possibly buoyancy-enhanced flow system beneath the slow spreading Mariana back-arc spreading center (see section 5.3.3).

6. Conclusions

[67] We present a 2-D seismic attenuation tomography profile across the Mariana subduction system. The attenuation tomography is based on t^*

measurements made for each earthquake-station pair along with simultaneous P wave corner frequency and seismic moment determination for each earthquake. In addition to investigating the effects of various earthquake source parameter assumptions, we also consider several frequency-dependent exponents ranging from 0 to 0.6. We find that path-averaged Q_P/Q_S ratios vary throughout the arc-back-arc system and that determining the optimal ratio by minimum misfit methods is highly subjective to the choice of frequency-dependent exponent and earthquake source assumptions. We invert ~2900 P and S t^* measurements separately for Q_P^{-1} and Q_P/Q_S structure and subsequently calculate Q_S^{-1}. Tomography results illuminate a low-attenuation slab and high-attenuation regions beneath the arc and the back-arc spreading center. Results show high attenuation beneath fore-arc seamounts and in the fore-arc region adjacent to the arc, which could be indicative of serpentinization or free fluids, although the attenuation effects of these processes are poorly understood at the present time. High attenuation within the subducting slab between ~50 and 100 km depth seems ubiquitous in subduction zones and may be indicative of fluids released from dehydrating minerals in the slab if free fluids are able to enhance attenuation.

[68] The island arc high-attenuation region is distinctly separate at shallow depths (<~50 km) from even higher attenuation beneath the back-arc spreading center. The two regions appear connected at ~75–100 km depth, which probably is the locus for volatile transfer between the slab and the back-arc spreading center. A ~75-km-wide columnar high-attenuation region persists beneath the back-arc spreading center to ~100–125 km depth. This columnar-shaped high-attenuation feature beneath the Mariana spreading center provides significant insight into slow spreading ridge dynamics, especially as compared to the much broader region of high attenuation found in previous studies of the fast spreading Lau back-arc spreading center, and the broad region of low seismic velocity found at the MELT region of the East Pacific Rise. Temperature estimates calculated from experimental results indicate that a thermal relaxation mechanism cannot be solely responsible for the high attenuation observed beneath both the arc and back-arc spreading center. We propose that the high attenuation beneath the Mariana arc is enhanced by hydration, and that the narrow zone of attenuation imaged at the spreading center results from a small region of enhanced melt production and high temperatures

beneath the ridge, which suggests the influence of buoyant flow in slow spreading center dynamics.

Acknowledgments

References

Aizawa, Y., A. Barnhoorn, U. H. Faul, J. D. Fitz Gerald, I. Jackson, and I. Kovács (2008), Seismic properties of Anita Bay dunite: An exploratory study of the influence of water, *J. Petrol.*, *49*, 841–855, doi:10.1093/petrology/egn007.

Aki, K. (1975), Origin of coda waves: Source, attenuation and scattering effects, *J. Geophys. Res.*, *80*, 3322–3342, doi:10.1029/JB080i023p03322.

Aki, K., and P. G. Richards (2002), *Quantitative Seismology*, 2nd ed., 700 pp., Univ. Sci. Books, Sausalito, Calif.

Anderson, J. G. (1986), Implication of attenuation for studies of earthquake sources, in *Earthquake Source Mechanics*, *Geophys. Monogr. Ser.*, vol. 37, edited by S. Das, J. Boatwright, and C. H. Scholz, pp. 311–318, AGU, Washington, D.C.

Anderson, J. G., and S. E. Hough (1984), A model for the shape of the Fourier amplitude spectrum of acceleration at high frequencies, *Bull. Seismol. Soc. Am.*, *74*, 1969–1993.

Baba, K., N. Seama, T. Goto, M. Ichiki, K. Schwalenberg, H. Utada, and K. Suyehiro (2004), Electrical structure of the upper mantle in the Mariana Subduction System, *Frontier Research on Earth Evolution* [*electronic*], vol. 2, Inst. for Res. on Earth Evol., Kanagawa, Japan. (Available at http://www.jamstec.go.jp/ifree/jp/05result/IFREE_Report_for_2003-2004/honbun/01_03.pdf)

Barazangi, M., W. Pennington, and B. Isacks (1975), Global study of seismic wave attenuation in the upper mantle behind island arcs using pP waves, *J. Geophys. Res.*, *80*(8), 1079–1092.

Barklage, M. E., J. A. Conder, D. A. Wiens, P. J. Shore, H. Shiobara, H. Sugioka, and H. Zhang (2006), 3-D seismic tomography of the Mariana mantle wedge from the 2003–2004 passive component of the Mariana Subduction Factory Imaging Experiment, *Eos Trans. American Geophysical Union*, *87*(52), Fall Meet. Suppl., Abstract T23C-0506.

Bowman, J. R. (1988), Body wave attenuation in the Tonga subduction zone, *J. Geophys. Res.*, *93*, 2125–2139, doi:10.1029/JB093iB03p02125.

Budiansky, B., E. E. Sumner, and R. J. O'Connell (1983), Bulk thermoelastic attenuation of composite materials, *J. Geophys. Res.*, *88*, 10,343–10,348.

Butler, R., C. S. McCreery, L. N. Frazer, and D. A. Walker (1987), High-frequency seismic attenuation of oceanic P and S waves in the western Pacific, *J. Geophys. Res.*, *92*, 1383–1396, doi:10.1029/JB092iB02p01383.

Conder, J. A. (2007), Temperature structure of the Mariana system from geodynamical modeling, paper presented at Subduction Factory Studies in the Izu-Bonin-Mariana Arc System: Results and Future Plans, MARGINS, Natl. Sci. Found., Honolulu, Hawaii.

Conder, J. A., and D. A. Wiens (2006), Seismic structure beneath the Tonga arc and Lau back-arc basin determined from joint Vp, Vp/Vs tomography, *Geochem. Geophys. Geosyst.*, *7*, Q03018, doi:10.1029/2005GC001113.

Conder, J. A., D. A. Wiens, and J. Morris (2002), On the decompression melting structure at volcanic arcs and back-arc spreading centers, *Geophys. Res. Lett.*, *29*(15), 1727, doi:10.1029/2002GL015390.

Dasgupta, R., M. M. Hirschmann, and N. D. Smith (2007), Water follows carbon: CO_2 incites deep silicate melting and dehydration beneath mid-ocean ridges, *Geology*, *35*, 135–138, doi:10.1130/G22856A.1.

de Moor, J. M., T. P. Fischer, D. R. Hilton, E. Hauri, L. A. Jaffe, and J. T. Camacho (2005), Degassing at Anatahan Volcano during the May 2003 eruption: implications from petrology, ash leachates, and SO_2 emissions, *J. Volcanol. Geotherm. Res.*, *146*, 117–138, doi:10.1016/j.jvolgeores.2004.11.034.

Der, Z. A. (1998), High-frequency P- and S-wave attenuation in the Earth, *Pure Appl. Geophys.*, *153*, 273–310, doi:10.1007/s000240050197.

Deshayes, P., P. Arroucau, T. Monfret, M. Pardo, J. Virieux, S. Beck, and G. Zandt (2007), Monte Carlo method to determine an initial model for seismic wave attenuation tomography: Application to the central Chile-Western Argentina (30–34°S) region, *Geophys. Res. Abstr.*, *9*, 04369.

Dunn, R. A., and D. W. Forsyth (2003), Imaging the transition between the region of mantle melt generation and the crustal magma chamber beneath the southern East Pacific Rise with short-period Love waves, *J. Geophys. Res.*, *108*(B7), 2352, doi:10.1029/2002JB002217.

Eberhart-Phillips, D., and M. Chadwick (2002), Three-dimensional attenuation model of the shallow Hikurangi subduction zone in the Raukumara Peninsula, New Zealand, *J. Geophys. Res.*, *107*(B2), 2033, doi:10.1029/2000JB000046.

Faul, U. H. (2001), Melt retention and segregation at mid-ocean ridges, *Nature*, *410*, 920–923, doi:10.1038/35073556.

Faul, U. H., and I. Jackson (2005), The seismological signature of temperature and grain size variations in the upper mantle, *Earth Planet. Sci. Lett.*, *234*, 119–134, doi:10.1016/j.epsl.2005.02.008.

Faul, U. H., J. D. Fitz Gerald, and I. Jackson (2004), Shear wave attenuation and dispersion in melt-bearing olivine polycrystals: 2. Microstructural interpretation and seismological implications, *J. Geophys. Res.*, *109*, B06202, doi:10.1029/2003JB002407.

Forsyth, D. W. (1996), Partial melting beneath a Mid-Atlantic Ridge segment detected by teleseismic PKP delays, *Geophys. Res. Lett.*, *23*, 463–466, doi:10.1029/96GL00379.

Forsyth, D. W., et al. (1998), Imaging the deep seismic structure beneath a mid-ocean ridge: The MELT experiment, *Science*, *280*, 1235–1238, doi:10.1126/science.280.5367.1235.

Fryer, P. (1996), Evolution of the Mariana convergent plate margin system, *Rev. Geophys.*, *34*, 89–125, doi:10.1029/95RG03476.

Goes, S., R. Govers, and P. Vacher (2000), Shallow mantle temperatures under Europe from P and S wave tomography, *J. Geophys. Res.*, *105*, 11,153–11,169.

Gribb, T. T., and R. F. Cooper (2000), The effect of an equilibrated melt phase on the shear creep and attenuation behavior of polycrystalline olivine, *Geophys. Res. Lett.*, *27*, 2341–2344, doi:10.1029/2000GL011443.

Gudmundsson, Ó., D. M. Finlayson, I. Itikarai, Y. Nishimura, and W. R. Johnson (2004), Seismic attenuation at Rabaul volcano, Papua new Guinea, *J. Volcanol. Geotherm. Res.*, *130*, 77–92, doi:10.1016/S0377-0273(03)00282-8.

Hacker, B. R., S. M. Peacock, G. A. Abers, and S. D. Holloway (2003), Subduction factory 2. Are intermediate-depth earthquakes in subducting slabs linked to metamorphic dehydration reactions?, *J. Geophys. Res.*, *108*(B1), 2030, doi:10.1029/2001JB001129.

Hammond, W. C., and D. R. Toomey (2003), Seismic velocity anisotropy and heterogeneity beneath the Mantle Electromagnetic and Tomography Experiment (MELT) region of the East Pacific Rise from analysis of P and S body waves, *J. Geophys. Res.*, *108*(B4), 2176, doi:10.1029/2002JB001789.

Hart, S. R. (1993), Equilibration during mantle melting: A fractal tree model, *Proc. Natl. Acad. Sci. U. S. A.*, *90*, 11,914–11,918, doi:10.1073/pnas.90.24.11914.

Helmberger, D. V. (1974), Generalized ray theory for shear dislocations, *Bull. Seismol. Soc. Am.*, *64*, 45–64.

Heuret, A., and S. Lallemand (2005), Plate motions, slab dynamics and back-arc deformation, *Phys. Earth Planet. Inter.*, *149*, 31–51, doi:10.1016/j.pepi.2004.08.022.

Hirschmann, M. M., C. Aubaud, and A. C. Withers (2005), Storage capacity of H_2O in nominally anhydrous minerals in the upper mantle, *Earth Planet. Sci. Lett.*, *236*, 167–181, doi:10.1016/j.epsl.2005.04.022.

Hough, S. E. (1996), Observational constraints on earthquake source scaling: Understanding the limits in resolution, *Tectonophysics*, *261*, 83–95, doi:10.1016/0040-1951(96)00058-3.

Hough, S. E., J. M. Lees, and F. Monastero (1999), Attenuation and source properties at the Coso geothermal area, California, *Bull. Seismol. Soc. Am.*, *89*, 1606–1619.

Hung, S. H., D. W. Forsyth, and D. R. Toomey (2000), Can a narrow, melt-rich, low-velocity zone of mantle upwelling be hidden beneath the East Pacific Rise? Limits from waveform modeling and the MELT Experiment, *J. Geophys. Res.*, *105*, 7945–7960, doi:10.1029/1999JB900316.

Hyndman, R. D., and S. M. Peacock (2003), Serpentinization of the forearc mantle, *Earth Planet. Sci. Lett.*, *212*, 417–432, doi:10.1016/S0012-821X(03)00263-2.

Jackson, I. (2007), Properties of rocks and minerals—Physical origins of anelasticity and attenuation in rock, in *Treatise on Geophysics*, edited by G. Schubert, pp. 493–525, Elsevier, Oxford, U.K.

Jackson, I., M. S. Paterson, and J. D. Fitz Gerald (1992), Seismic wave dispersion and attenuation in Aheim dunite: An experimental study, *Geophys. J. Int.*, *108*, 517–534, doi:10.1111/j.1365-246X.1992.tb04633.x.

Jackson, I., J. D. FitzGerald, U. H. Faul, and B. H. Tan (2002), Grain-size-sensitive seismic wave attenuation in polycrystalline olivine, *J. Geophys. Res.*, *107*(B12), 2360, doi:10.1029/2001JB001225.

Jackson, I., U. H. Faul, J. D. Fitz Gerald, and S. J. S. Morris (2006), Contrasting viscoelastic behavior of melt-free and melt-bearing olivine: Implications for the nature of grain-boundary sliding, *Mater. Sci. Eng. A*, *442*, 170–174, doi:10.1016/j.msea.2006.01.136.

Jackson, I., A. Barnhoorn, Y. Aizawa, and C. Saint (2008), Improved procedures for the laboratory study of high-temperature viscoelastic relaxation, *Phys. Earth Planet. Inter.*, *172*(1–2), 104–115.

Jackson, I., A. Barnhoorn, Y. Aizawa, and C. Saint (2009), Improved procedures for the laboratory study of high-temperature viscoelastic relaxation, *Phys. Earth Planet. Inter.*, *172*, 104–115, doi:10.1016/j.pepi.2008.03.010.

Kanamori, H., and D. L. Anderson (1975), Theoretical basis of some empirical relations in seismology, *Bull. Seismol. Soc. Am.*, *65*, 1073–1095.

Kanamori, H., and G. S. Stewart (1976), Mode of the strain release along the Gibbs fracture zone, Mid-Atlantic ridge, *Phys. Earth Planet. Inter.*, *11*, 312–332, doi:10.1016/0031-9201(76)90018-2.

Karato, S. (2003), Mapping water content in the upper mantle, in *Inside the Subduction Factory*, *Geophys. Monogr. Ser.*, vol. 138, edited by J. Eiler, pp. 135–152, AGU, Washington, D.C.

Kato, T., J. Beavan, T. Matsushima, Y. Kotake, J. T. Camacho, and S. Nakao (2003), Geodetic evidence of back-arc spreading in the Mariana Trough, *Geophys. Res. Lett.*, *30*(12), 1625, doi:10.1029/2002GL016757.

Kelley, K. A., T. Plank, S. Newman, E. M. Stolper, T. L. Grove, S. Parman, and E. Hauri (2003), Mantle melting as a function of water content in arcs, *Eos Trans. American Geophysical Union*, *84*(46), Fall Meet. Suppl., Abstract V41D-06.

Kelley, K. A., T. Plank, T. L. Grove, E. M. Stolper, S. Newman, and E. Hauri (2006), Mantle melting as a function of water content beneath back-arc basins, *J. Geophys. Res.*, *111*, B09208, doi:10.1029/2005JB003732.

Kern, H., B. Liu, and T. Popp (1997), Relationship between anisotropy of P and S wave velocities and anisotropy of attenuation in serpentinite and amphibolite, *J. Geophys. Res.*, *102*, 3051–3065, doi:10.1029/96JB03392.

Kitada, K., N. Seama, T. Yamazaki, Y. Nogi, and K. Suyehiro (2006), Distinct regional differences in crustal thickness along the axis of the Mariana Trough, inferred from gravity anomalies, *Geochem. Geophys. Geosyst.*, *7*, Q04011, doi:10.1029/2005GC001119.

Klein, E. M., and C. H. Langmuir (1987), Global correlations of ocean ridge basalt chemistry with axial depth and crustal thickness, *J. Geophys. Res.*, *92*, 8089–8115, doi:10.1029/JB092iB08p08089.

Knopoff, L. (1964), Q, *Rev. Geophys.*, *2*, 625–660, doi:10.1029/RG002i004p00625.

Langmuir, C. H., E. M. Klein, and T. Plank (1992), Petrological systematics of mid-ocean ridge basalts: Constraints on melt generation beneath ocean ridges, in *Mantle Flow and Melt Generation at Mid-Ocean Ridges*, *Geophys. Monogr. Ser.*, vol. 71, edited by J. Phipps Morgan, D. K. Blackman, and J. M. Sinton, pp. 183–280, AGU, Washington, D.C.

Lundstrom, C. C., Q. Williams, and J. Gill (1998), Investigating solid mantle upwelling rates beneath mid-ocean ridges using U-series disequilibria: I. A global approach, *Earth Planet. Sci. Lett.*, *157*, 151–165, doi:10.1016/S0012-821X(98)00038-7.

Madariaga, R. (1976), Dynamics of an expanding circular fault, *Bull. Seismol. Soc. Am.*, *66*, 639–666.

Madge, L. S., and D. W. Sparks (1997), Three-dimensional mantle upwelling, melt generation, and melt migration beneath segment slow spreading ridges, *J. Geophys. Res.*, *102*, 20,571–20,583.

Menke, W. (1984), *Geophysical Data Analysis: Discrete Inverse Theory*, 260 pp., Academic, London.

Nakajima, J., Y. Takei, and A. Hasegawa (2005), Quantitative analysis of the inclined low-velocity zone in the mantle wedge of northeastern Japan: A systematic change of melt-filled pore shapes with depth and its implications for melt migration, *Earth Planet. Sci. Lett.*, *234*, 59–70, doi:10.1016/j.epsl.2005.02.033.

Nakamura, R., K. Statake, S. Toda, T. Uetake, and S. Kamiya (2006), Three-dimensional attenuation (Qs) structure beneath the Kanto District, Japan, as inferred from strong motion records, *Geophys. Res. Lett.*, *33*, L21304, doi:10.1029/2006GL027352.

Park, J., C. R. Lindberg, and F. L. I. Vernon (1987), Multitaper spectral analysis of high frequency seismograms, *J. Geophys. Res.*, *92*, 12,675–12,684, doi:10.1029/JB092iB12p12675.

Parmentier, E. M., and J. Phipps Morgan (1990), Spreading rate dependence of three-dimensional structure in oceanic spreading centers, *Nature*, *348*, 325–328, doi:10.1038/348325a0.

Peacock, S. M., P. E. van Keken, S. D. Holloway, B. R. Hacker, G. A. Abers, and R. L. Fergason (2005), Thermal structure of the Costa Rica–Nicaragua subduction zone, *Phys. Earth Planet. Inter.*, *149*, 187–200, doi:10.1016/j.pepi.2004.08.030.

Pearce, J. A., and R. J. Stern (2006), The origin of back-arc basin magmas: Trace element and isotope perspectives, in *Back-Arc Spreading Systems: Geological, Biological, Chemical, and Physical Interactions*, Geophys. Monogr. Ser., vol. 166, edited by D. M. Christie et al., pp. 63–86, AGU, Washington, D. C.

Pearce, J. A., R. J. Stern, S. H. Bloomer, and P. Fryer (2005), Geochemical mapping of the Mariana arc-basin system: Implications for the nature and distribution of subduction components, *Geochem. Geophys. Geosyst.*, *6*, Q07006, doi:10.1029/2004GC000895.

Pozgay, S. H. (2007), *Seismic Investigations of the Mariana Subduction System: Anisotropy, Attenuation, and Volcano Seismology*, 220 pp., Washington Univ. in St. Louis, St. Louis, Mo.

Pozgay, S. H., D. A. Wiens, H. Shiobara, and H. Sugioka (2007), Complex mantle flow in the Mariana subduction system: Evidence from shear wave splitting, *Geophys. J. Int.*, *170*, 371–386, doi:10.1111/j.1365-246X.2007.03433.x.

Quinlan, D. M. (1995), *Antelope*, Boulder Real Time Technol. Inc., Boulder, Colo.

Roth, E. G., D. A. Wiens, L. M. Dorman, J. Hildebrand, and S. C. Webb (1999), Seismic attenuation tomography of the Tonga-Fiji region using phase pair methods, *J. Geophys. Res.*, *104*(B3), 4795–4809.

Rüpke, L. H., J. P. Morgan, M. Hort, and J. A. D. Connolly (2004), Serpentine and the subduction zone water cycle, *Earth Planet. Sci. Lett.*, *223*, 17–34, doi:10.1016/j.epsl.2004.04.018.

Rychert, C. A., K. M. Fischer, D. G. A. Abers, T. Plank, E. Syracuse, J. M. Protti, V. Gonzalez, and W. Strauch (2008), Strong along-arc variations in attenuation in the mantle wedge beneath Costa Rica and Nicaragua, *Geochem. Geophys. Geosyst.*, *9*, Q10S10, doi:10.1029/2008GC002040.

Sato, H., I. S. Sacks, T. Muraswe, G. Munchill, and H. Fukuyama (1989), Qp-melting temperature relation in peridotite at high pressure and temperature: Attenuation mechanism and implications for the mechanical properties of the upper mantle, *J. Geophys. Res.*, *94*, 10,647–10,661.

Schlotterbeck, B. A., and G. A. Abers (2001, Three-dimensional attenuation variations in southern California, *J. Geophys. Res.*, *106*, 30,719–30,735, doi:10.1029/2001JB000237.

Scholz, C. H., and J. Campos (1995), On the mechanism of seismic decoupling and back arc spreading at subduction zones, *J. Geophys. Res.*, *100*, 22,103–22,115.

Schurr, B., G. Asch, A. Rietbrock, R. Trumbull, and C. Haberland (2003), Complex patterns of fluid and melt transport in the central Andean subduction zone revealed by attenuation tomography, *Earth Planet. Sci. Lett.*, *215*, 105–119, doi:10.1016/S0012-821X(03)00441-2.

Shaw, A. M., E. H. Hauri, T. Fischer, D. R. Hilton, and K. A. Kelley (2008), Hydrogen isotopes in Mariana arc melt inclusions: Implications for subduction dehydration and the deep-Earth water cycle, *Earth Planet. Sci. Lett.*, *275*(1–2), 138–145.

Shen, Y., and D. W. Forsyth (1995), Geochemical constraints on initial and final depths of melting beneath mid-ocean ridges, *J. Geophys. Res.*, *100*, 2211–2237, doi:10.1029/94JB02768.

Shiobara, H., and T. Kanazawa (2008), Development of a light weight and autonomic sensor system for ocean bottom seismometer, (in Japanese), *Zisin*, *2*, 61.

Shiobara, H., H. Sugioka, K. Mochizuki, S. Oki, T. Kanazawa, Y. Fukao, and K. Suyehiro (2005), Long term seismic observation in Mariana by OBSs: Double seismic zone and upper mantle structure, *Eos Trans. American Geophysical Union*, *86*(52), Fall Meet. Suppl., Abstract T53A-1407.

Shito, A., and T. Shibutan (2003a), Anelastic structure of the upper mantle beneath the northern Philippine Sea, *Phys. Earth Planet. Inter.*, *140*, 319–329, doi:10.1016/j.pepi.2003.09.011.

Shito, A., and T. Shibutan (2003b), Nature of heterogeneity of the upper mantle beneath the northern Philippine Sea as inferred from attenuation and velocity tomography, *Phys. Earth Planet. Inter.*, *140*, 331–341, doi:10.1016/j.pepi.2003.09.010.

Shito, A., S. Karato, and J. Park (2004), Frequency dependence of Q in Earth's upper mantle inferred from continuous spectra of body waves, *Geophys. Res. Lett.*, *31*, L12603, doi:10.1029/2004GL019582.

Shito, A., S.-I. Karato, K. N. Matsukage, and Y. Nishibara (2006), Towards mapping the three-dimensional distribution of water in the upper mantle from velocity and attenuation tomography, in *Earth's Deep Water Cycle*, Geophys. Monogr. Ser., vol. 168, edited by S. D. Jacobsen and S. vanderLee, pp. 225–236, AGU, Washington, D. C.

Sparks, D. W., and E. M. Parmentier (1991), Melt extraction from the mantle beneath spreading centers, *Earth Planet. Sci. Lett.*, *105*, 368–377, doi:10.1016/0012-821X(91)90178-K.

Spiegelman, M., and D. P. McKenzie (1987), Simple 2-D models for melt extraction at mid-ocean ridges and island arcs, *Earth Planet. Sci. Lett.*, *83*, 137–152, doi:10.1016/0012-821X(87)90057-4.

Stachnik, J. C. (2002), *Seismic Attenuation in Central Alaska*, 130 pp., Boston Univ, Boston, Mass.

Stachnik, J. C., G. A. Abers, and D. H. Christensen (2004), Seismic attenuation and mantle wedge temperatures in the Alaska subduction zone, *J. Geophys. Res.*, *109*, B10304, doi:10.1029/2004JB003018.

Su, W., and R. Buck (1993), Buoyancy effects on mantle flow under mid-ocean ridges, *J. Geophys. Res.*, *98*, 12,191–12,205.

Takahashi, N., S. Kodaira, S. L. Klemperer, Y. Tatsumi, Y. Kaneda, and K. Suyehiro (2007), Crustal structure and evolution of the Mariana intra-oceanic island arc, *Geology*, *35*, 203–206, doi:10.1130/G23212A.1.

Takanami, T., I. Selwyn Sacks, and A. Hasegawa (2000), Attenuation structure beneath the volcanic front in northeastern

Japan from broad-band seismograms, *Phys. Earth Planet. Inter.*, *121*, 339–357, doi:10.1016/S0031-9201(00)00169-2.

Thomson, D. J. (1982), Spectrum estimation and harmonic analysis, *Proc. IEEE*, *70*, 1055–1096, doi:10.1109/PROC.1982.12433.

Tibi, R., D. A. Wiens, and X. Yuan (2008), Seismic evidence for widespread serpentinized forearc mantle along the Mariana convergence margin, *Geophys. Res. Lett.*, *35*, L13303, doi:10.1029/2008GL034163.

Tsumura, N., S. Matsumoto, S. Horiuchi, and A. Hasegawa (2000), Three-dimensional attenuation structure beneath the northeastern Japan arc estimated from spectra of small earthquakes, *Tectonophysics*, *319*, 241–260, doi:10.1016/S0040-1951(99)00297-8.

Turner, S., P. J. Evans, and C. J. Hawkesworth (2001), Ultra-fast source-to-surface movement of melt at island ARCS from 226Ra-230Th systematics, *Science*, *292*, 1363–1366, doi:10.1126/science.1059904.

Um, J., and C. H. Thurber (1987), A fast algorithm for two-point seismic ray tracing, *Bull. Seismol. Soc. Am.*, *77*, 972–986.

Vaišnys, J. R. (1968), Propagation of acoustic waves through a system undergoing phase transformations, *J. Geophys. Res.*, *73*, 7675–7683, doi:10.1029/JB073i024p07675.

van der Hilst, R. D., E. R. Engdahl, W. Spakman, and G. Nolet (1991), Tomographic imaging of subducted lithosphere below northwest Pacific island arcs, *Nature*, *353*, 37–43, doi:10.1038/353037a0.

Warren, L. M., and P. M. Shearer (2002), Mapping lateral variations in upper mantle attenuation by stacking *P* and *PP* spectra, *J. Geophys. Res.*, *107*(B12), 2342, doi:10.1029/2001JB001195.

Wiens, D. A., H. Shiobara, S. H. Pozgay, M. E. Barklage, E. L. Emry, D. S. Heeszel, M. Pyle, J. A. Conder, and H. Sugioka (2005), An overview of the 2003–2004 Mariana Subduction Factory Passive Imaging Experiment, *Eos Trans. American Geophysical Union*, *86*(52), Fall Meet. Suppl., Abstract T44A–04.

Wiens, D. A., K. A. Kelley, and T. Plank (2006), Mantle temperature variations beneath back-arc spreading centers inferred from seismology, petrology, and bathymetry, *Earth Planet. Sci. Lett.*, *248*, 30–42, doi:10.1016/j.epsl.2006.04.011.

Wiens, D. A., J. A. Conder, and U. H. Faul (2008), The seismic structure and dynamics of the mantle wedge, *Annu. Rev. Earth Planet. Sci.*, *36*, 421–455, doi:10.1146/annurev.earth.33.092203.122633.

Yang, Y., D. W. Forsyth, and D. S. Weeraratne (2007), Seismic attenuation near the East Pacific Rise and the origin of the low-velocity zone, *Earth Planet. Sci. Lett.*, *258*, 260–268, doi:10.1016/j.epsl.2007.03.040.

Zhang, H., C. H. Thurber, D. R. Shelly, S. Ide, G. C. Bereoza, and A. Hasegawa (2004), High-resolution subducting-slab structure beneath northern Honshu, Japan, revealed by double-difference tomography, *Geology*, *32*, 361–364, doi:10.1130/G20261.2.

Zhao, D., A. Hasegawa, and S. Horiuchi (1992), Tomographic imaging of P and S wave velocity structure beneath northeastern Japan, *J. Geophys. Res.*, *97*, 19,909–19,928.